Contributions to Mineralogy and Petrology (2021) 176:68
https://doi.org/10.1007/s00410-021-01827-z

ORIGINAL PAPER

Apatite as an alternative petrochronometer to trace the evolution of magmatic systems containing metamict zircon

Hao-Cheng Yu[1] · **Kun-Feng Qiu**[1,2,3] · **Callum J. Hetherington**[4] · **David Chew**[5] · **Ya-Qi Huang**[1] · **Deng-Yang He**[1] · **Jian-Zhen Geng**[6] · **Hai-Yang Xian**[2]

Received: 17 March 2021 / Accepted: 9 August 2021 / Published online: 19 August 2021

Abstract

Obtaining reliable petrochronological and geochemical data from metamict zircon may be challenging. Metamict zircon and crystalline apatite from the *Meiwu granodiorite* and its microgranular enclaves from the Paleo-Tethys belt are examined to constrain their crystallization ages and the genetic mechanism of related skarn mineralization. The metamict zircon yields highly disturbed ^{206}Pb/^{238}U dates. Transmission electron microscopy shows that radiation damage forms nanoscale-banded damaged zones, leading to spurious dates. The coexisting apatite has not accumulated radiation damage, and apatite crystals from the granodiorite and its enclaves yield reasonably precise LA-ICPMS U–Pb Tera–Wasserburg concordia lower intercept dates of 240.2 ± 3.8 and 239.9 ± 4.0 Ma (2σ), with MSWDs of 1.0 and 2.1. Considering the fast cooling of the granite, the U–Pb dates effectively represent crystallization ages for these rocks. Compositional analysis shows that there are no Ce anomalies in apatite in either the granodiorite or enclave, indicating low oxygen fugacities. Apatite crystals from enclaves have weaker negative Eu anomalies, higher Sr, and lower HREE and Y contents than those in granodiorite. The compositions confirm enclaves as products of water-rich melts, resulting in amphibole fractionation and suppression of plagioclase crystallization. The hydrous magma induced production of hydrothermal-fluids that mobilized metals dispersed in dry magma and concentrated them into mineralization traps, which contributed to the formation of widespread skarns in Paleo-Tethys belt. This study demonstrates that apatite is effective in tracing the evolution of magmatic systems containing metamict zircon.

Keywords Apatite petrochronology and geochemistry · Zircon radiation damage · Magma mixing · Skarn mineralization · Paleo-Tethys

Introduction

There have been considerable advances in the field of in-situ U–Pb geochronology since the first laser ablation–inductively coupled plasma mass spectrometry system (LA–ICPMS) was developed (Gray 1985). These systems offer rapid acquisition of large datasets compared to isotope dilution-thermal ionization mass spectrometry or ion microprobe U–Pb methods, and have led to significant advances in placing temporal constraints on geological processes (Chew et al. 2014; Spencer et al. 2016). Zircon is undoubtedly the most popular U–Pb geochronometer, in part due to its

---

Communicated by Daniela Rubatto.

✉ Kun-Feng Qiu
KunfengQiu@qq.com

[1] State Key Laboratory of Geological Processes and Mineral Resources, School of Earth Sciences and Resources, China University of Geosciences (Beijing), No. 29 Xueyuan Road, Haidian District, Beijing 100083, China

[2] CAS Key Laboratory of Mineralogy and Metallogeny/Guangdong Provincial Key Laboratory of Mineral Physics and Materials, Guangzhou Institute of Geochemistry, Chinese Academy of Sciences (CAS), Guangzhou 510640, China

[3] CAS Key Laboratory of Ore Deposit Geochemistry, Guiyang Institute of Geochemistry, Chinese Academy of Sciences (CAS), Guiyang 550000, China

[4] Department of Geosciences, Texas Tech University, Lubbock, TX 79409, USA

[5] Department of Geology, Trinity College Dublin, Dublin 2, Ireland

[6] Isotopic Laboratory, Tianjin Center, China Geological Survey, Tianjin 300100, China

extremely high closure temperature and negligible common Pb contents (Spencer et al. 2016; Rubatto 2017). Although zircon represents generally a very U–Pb robust chronometer, metamictization of the zircon lattice from radioactive decay of U and Th, may be particularly pronounced in older zircon and/or in zircon with high actinide abundances. Metamictization may disrupt the U-(Th)-Pb isotope system and lead to Pb loss or gain, increasing the uncertainty and imprecision on a U-(Th)-Pb date (Corfu et al. 2003; Nasdala et al. 2004; Utsunomiya et al. 2004; Gao et al. 2014; Li 2016). Zircon with high U and Th contents, therefore, present many challenges as a geochronometer (Kogawa et al. 2012).

Apatite is another ubiquitous accessory mineral in many rocks, especially Ca-rich igneous and metamorphic rocks, as P_2O_5 has a low solubility in silicate melts and only a small amount of phosphorus may enter the crystal lattices of other rock-forming minerals (Chew et al. 2011; Cao et al. 2012; Chew and Spikings 2015; Pochon et al. 2016; Szopa et al. 2020). The abundance of apatite and its ability to incorporate some U and rare earth elements (REEs) make it is widely employed in U–Pb, Lu–Hf, and low-temperature thermochronology studies (Chew et al. 2011; Chew and Spikings 2015; Cao et al. 2019; Konecke et al. 2019). The typical high abundances of REEs along with Sr, and other trace elements, make it a powerful tool for tracing the source and evolution of geological systems (Gregory et al. 2009; Mao et al. 2016; Hughes et al. 2018; O'Sullivan et al. 2018; Hu et al. 2020; Yu et al. 2020a). The challenges of U–Pb dating of apatite include high common Pb/radiogenic Pb ratios and, in addition to volume diffusion at significantly lower temperatures than zircon, Pb mobilization mechanisms can be associated with fluids and ‘fast pathway’ diffusion through cracks/fractures and dislocations (Kirkland et al. 2018). Strategies to minimize the impact of these challenges include enhanced common Pb correction procedures and detailed textural observations via cathodoluminescence (CL) and back-scattered electron (BSE) imaging to improve laser-spot placement and data interpretation (Chew et al. 2011; Kirkland et al. 2018).

Granitoids with abundant microgranular enclaves and related skarns are widespread in the Paleo-Tethys belt. Previous researchers have proposed that they were derived from magma mixing between mafic and felsic magmas (Luo et al. 2015). Such processes also caused extensive skarn mineralization and are associated with elevated oxygen fugacity as evidenced by zircon oxygen fugacity determinations from microgranular enclaves (Qiu and Deng 2017). Nevertheless, zircon from microgranular enclaves may not be suitable for calculations of oxygen fugacity because the exact composition of the parental magma, which is necessary for constraining magma oxygen fugacity, is unknown due to the assimilation of surrounding rocks (Yu et al. 2019; Zou et al. 2019). In addition, light rare earth elements (LREEs) are preferentially incorporated into damaged lattice sites of zircon during subsequent geological events, restricting the application of metamict zircon as an oxy-barometer (Whitehouse and Kamber 2002). As a result, the role of magma mixing in skarn mineralization in Paleo-Tethys rocks in the West Qinling is unknown. Metamict zircon and crystalline apatite from the *Meiwu granodiorite* and its microgranular enclaves in the West Qinling, central China, were subjected to LA-(MC)ICPMS U–Pb isotope dating. The crystal structures of zircon and apatite were identified by Raman spectroscopy and transmission electron microscopy (TEM). In addition, trace element abundances of apatite were analyzed for tracing the evolution of magmatic systems. The main contributions of this paper are twofold. First, we suggest apatite as an alternative petrochronometer in igneous rocks containing metamict zircon; and second, this study increases our knowledge of the petrogenetic processes responsible for the genesis of the Triassic granitoids and their contributions to skarn mineralization in the Paleo-Tethys belt.

Regional geology

The West Qinling orogen in central China between the North China and the South China blocks, including the North Qinling and South Qinling terranes, has a complex geological history (Fig. 1a; Dong et al. 2011a, b; Deng and Wang 2016). In the Paleozoic, oceanic crust of the Shangdan ocean underwent northward subduction beneath the North Qinling terrane at ca. 540 Ma, which is constrained by U–Pb zircon geochronology from subduction-related rocks (Dong et al. 2011b). It is inferred that the Shangdan ocean finally closed in the Early Devonian based on the widespread unconformity between the middle Devonian and older strata in the South Qinling terrane (Yang et al. 2015a; Dong and Santosh 2016; Yu et al. 2019; Deng et al. 2021). The Mianlue ocean, a branch of the Paleo-Tethys started spreading in the Silurian resulting in separation of the South Qinling terrane from the South China block (Dong and Santosh 2016; Deng et al. 2018). LA-ICPMS U–Pb ages of 300 to 250 Ma from arc-related anorthosite, andesite, and diabase have been interpreted to date the onset of subduction of the Mianlue ocean along the Animaqing-Mianlue suture (Fig. 1a; Dong et al. 2016). Upper Triassic or Upper Triassic to Jurassic foreland molasse basins and NW-oriented fold and thrust fault systems mark the final closure of the Mianlue ocean (Fig. 1a; Yang et al. 2015b; Dong and Santosh 2016). This model is also supported by the widespread emplacement of granitoids (Fig. 1a; Li et al. 2015; Yu et al. 2019). I-type granites with ages of ca. 250 to 235 Ma show arc-related geochemical features, corresponding to a subduction setting (Li et al. 2015; Qiu and Deng 2017). The granitoids ranging from 228 to 215 Ma

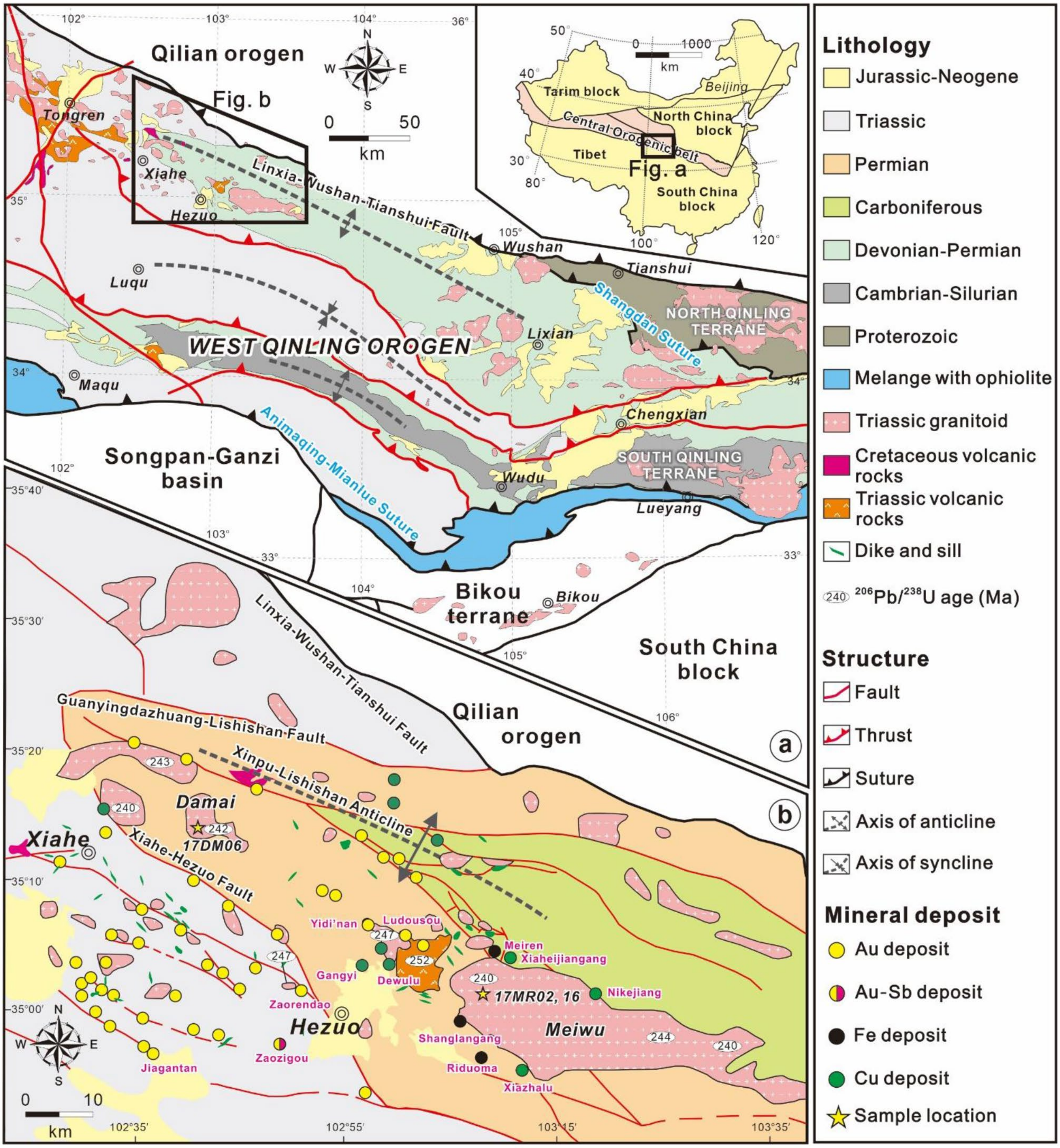

Fig. 1 **a** Major tectonic domains of the West Qinling in China. The inset shows the location of the study area (modified after Qiu et al. 2020). **b** Simplified geological map of the Xiahe–Hezuo polymetallic district, showing the distribution of Triassic granitoids and mineral systems (modified after Qiu and Deng 2017)

are enriched in large ion lithophile elements and the LREE and depleted in the high field-strength elements Nb and Ta, indicating they derived from thickened crust, likely in a syn-collisional setting (Dong and Santosh 2016; Geng et al. 2017). Post-Triassic intercontinental deformation, orogenic collapse and subsidence occurred from ca. 215 to 185 Ma (Yu et al. 2020b). Rapakivi granitoids emplaced from 215 to 185 Ma show features of I- to A-type granites, suggesting an extensional setting during the post-collision stage (Dong and Santosh 2016).

Petrology and related Skarn mineralization

The Xiahe–Hezuo polymetallic district is situated in the northwesterly part of the West Qinling orogen (Fig. 1). Widespread granitic bodies are typically elliptical in map view and define a total exposed area of approximately 700 km^2 (Fig. 1b). They generally consist of medium- to fine-grained biotite granodiorite, biotite quartz diorite and biotite quartz diorite porphyry, and intrude Carboniferous to Triassic greenschist-facies slate and carbonate rocks. Numerous studies have shown that these granitoids were mainly emplaced at 250–235 Ma during northward subduction of the Paleo-Tethys oceanic slab and are discontinuously distributed in a NW–SE direction (Li et al. 2015; Qiu and Deng 2017; Yu et al. 2019).

The Damai stock is located 20 km east of the city of Xiahe adjacent to the NW–SE trending Xiahe-Hezuo and Guanyindashan-Lishishan faults (Fig. 1b). It was intruded into Permian slates with a total outcrop area of about 30 km^2 (Fig. A.1a). The pluton is mainly composed of granodiorite (Fig. A.1b) that is fine- to medium-grained with a massive structure. It is mainly composed of quartz (10–50%), plagioclase (20–50%), biotite (10–25%), amphibole (10–20%), and K-feldspar (5–20%) (Fig. A.1c, d), with apatite, zircon, and monazite as minor constituents.

The Meiwu batholith, with an area of 423 km^2, is located 20 km east of the Hezuo city. It crops out adjacent to the Xinpu-Lishishan anticline and intruded Carboniferous and Permian metasediments (Figs. 1, 2). The pluton is mainly composed of medium-grained monzogranite, granodiorite, biotite quartz diorite, and microgranular enclaves. The granodiorite constitutes the major phase of the Meiwu batholith, and contains plagioclase (30–45%), quartz (20–35%), K-feldspar (10–15%), biotite (5–15%), amphibole (5%) (Fig. 3a). Microgranular enclaves ranging from 5 to 50 cm in diameter occasionally occur in the biotite granodiorite. The granodiorite becomes porphyritic near the enclaves (Fig. 3b). The quartz is fine-grained and accounts for up to 30% of the matrix. Quartz phenocrysts in the granodiorite are comprised of rounded cores, surrounded by rims in optical continuity with the core but with fine-grained quartz inclusions (Fig. 3c). Enclaves are abundant in the granodiorite, ranging from a few centimeters to tens of meters in diameter, with sharp contacts (Figs. 2a–d, 3d). They sometimes contain back veins and capture quartz and plagioclase xenocrysts (Fig. 2b–f). Quartz megacrysts surrounded by amphibole and biotite are common in the enclaves (Fig. 3e). Euhedral to subhedral plagioclase xenocrysts show sieved-textured cores filled with fine-grained biotite, amphibole, and apatite, and smooth rims with resorption boundaries between cores and rims (Fig. 3d, f). In some cases, glomerocrysts of amphibole and biotite give the rocks a glomeroporphyritic texture (Fig. 3g). Apatite is a common accessory mineral in the enclaves, occurring as columnar and acicular crystals (Fig. 3f, h).

Several skarn deposits genetically related to the Meiwu batholith occur along the margins of the batholith in the Permian carbonate, including the Meiren, Shanglanggang, and Riduoma iron deposits and the Xiaheijiangang, Nikejiang, and Xiazhalu copper deposits (Fig. 1). The Meiren iron deposit is located in the northeastern part of the Meiwu batholith (Fig. 1; Luo et al. 2015; Qiu et al. 2021a). The skarns are generated by contact metamorphism from the thermal effects of the intrusion (Li et al. 2019; Hu et al. 2020). Four stages of skarn and ore formation in the Meiren deposit associated with the Meiwu batholith were: (I) prograde skarn (garnet-diopside-wollastonite); (II) retrograde skarn (amphibole-epidote-phlogopite-magnetite); (III) sulfide (chalcopyrite-pyrite-quartz); and (IV) carbonate (calcite) (Qiu and Deng 2017; Sui et al. 2017). The prograde skarn stage is intensely developed within the granodiorite and sedimentary rocks. It formed under higher temperature and has a generally anhydrous mineral assemblage that contains diopside, garnet, and wollastonite. The retrograde skarn stage is characterized by a lower temperature and generally hydrous minerals (Meinert et al. 2005; Qiu and Deng 2017). The main Fe mineralization phase is associated with the retrograde skarn stage, and magnetite is the predominant mineral in the massive ores (Qiu et al. 2021a). The sulfide stage is represented by widely distributed quartz-pyrite veins, which were then cut by calcite veins associated with the carbonate stage.

Sampling and analytical procedures

Sample description and mineral separation

One granodiorite sample of the Damai pluton was collected (Fig. A.1d). Two representative samples of the granodiorite and the microgranular enclaves of the Meiwu pluton were also investigated (Fig. 2e, f). The sample locations and petrography are summarized in Table 1. The three samples were crushed and disaggregated to 40–60 mesh and zircon and apatite crystals were separated using conventional sieving, and magnetic and heavy liquid separation methods at the Langfang Regional Geological Survey, Hebei Province, China. Zircon and apatite separates were handpicked from the mineral separates under a binocular microscope on the basis of size, color, and morphology. The handpicked separates were then mounted in epoxy resin and polished down to near half sections to expose internal structures. Polished

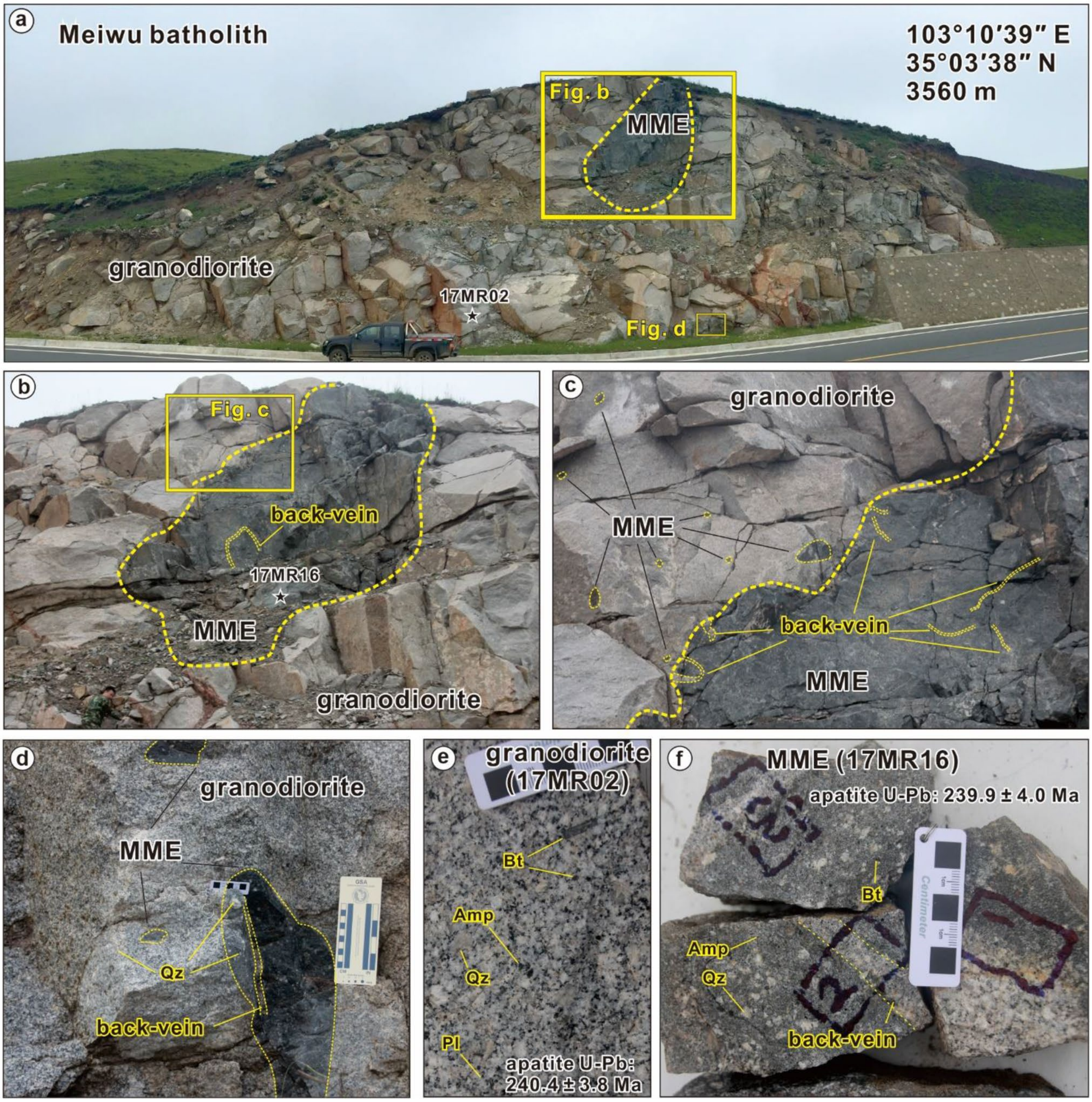

Fig. 2 **a** Outcrop of the Meiwu batholith. **b–d** Sharp contact between granodiorite and hosting microgranular enclaves. **e** Hand specimen of granodiorite (17MR02). **f** Hand specimen of microgranular enclaves capturing quartz and plagioclase xenocrysts (17MR16)

mounts were carbon coated for CL and BSE imaging. The CL and BSE images for zircon and apatite were obtained using a Tescan MIRA3 field-emission scanning electron microscope under operating conditions of 10 kV and 20 nA at Langfang Tuoxuan Rock and Mineral Testing Service Co., Ltd., China. The imaging techniques were used to identify domains within zircon and apatite grains without inclusions or cracks for micro-analysis.

Zircon and apatite LA–(MC)–ICPMS U–Pb dating

Zircon and apatite U–Pb isotope analyses were conducted by LA–(MC)–ICPMS at the Isotopic Laboratory, Tianjin Center, China Geological Survey. Zircon dating was performed by a Neptune double focusing multiple-collector coupled to a NEW WAVE 193 nm-FX ArF Excimer laser-ablation system. Apatite dating was performed using an Agilent 7900 ICPMS coupled to a RESOlution-LR 193 nm-FX ArF

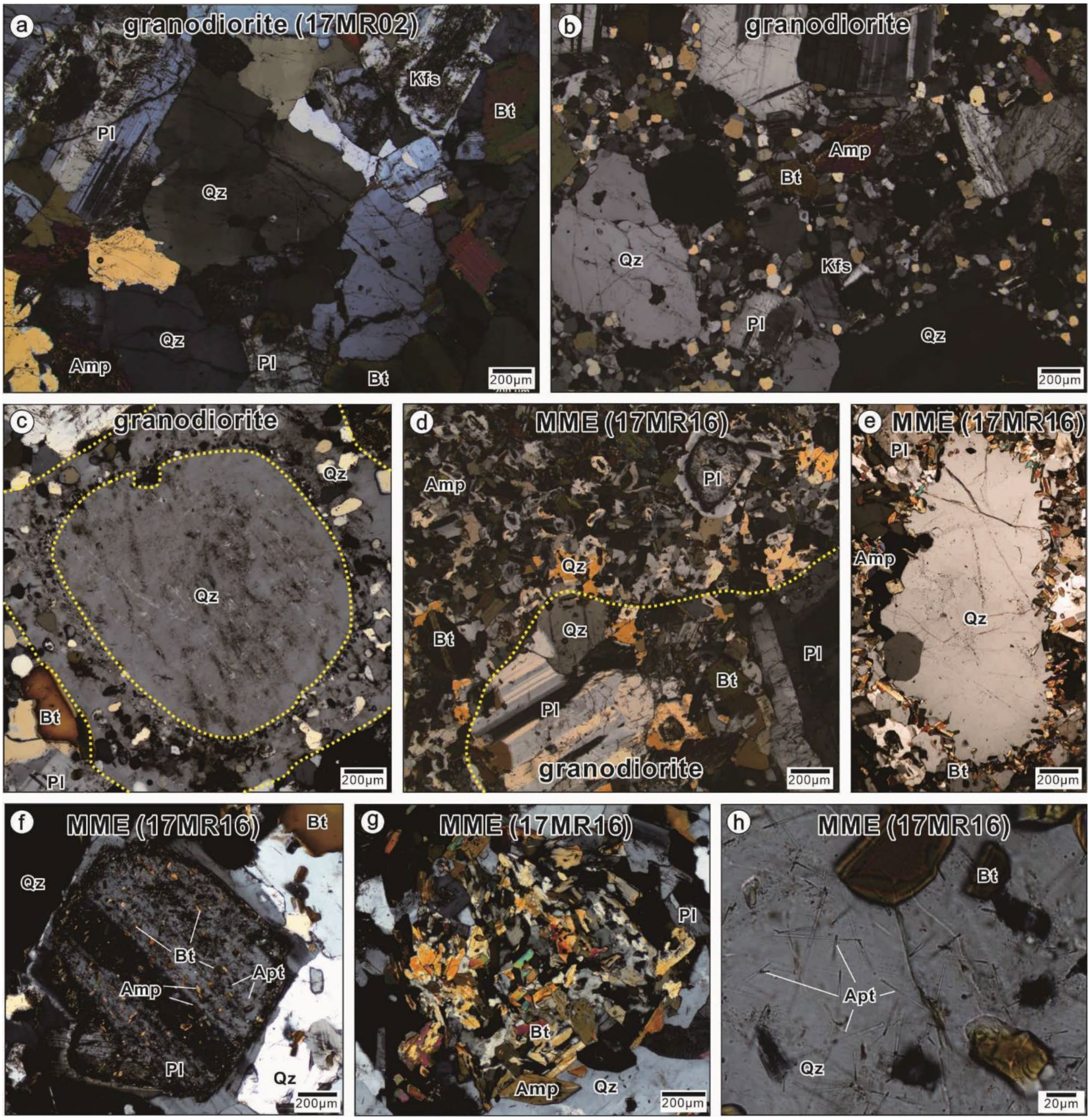

Fig. 3 **a** Granodiorite at Meiwu contains plagioclase, quartz, K-feldspar, biotite, and amphibole. **b** Texture of granodiorite turns porphyritic near the enclaves. **c** The quartz phenocryst in granodiorite contains fine-grained quartz grains in the square quartz rim and a medium-grained round quartz core. **d** Sharp contact between granodiorite and hosting microgranular enclaves. **e** Quartz megacryst is surrounded by amphibole and biotite in the enclave. **f** Plagioclase xenocrysts show sieved textural cores filling with fine-grained biotite, amphibole, and apatite, and smooth rims, with resorption boundaries between cores and rims in the enclave. **g** Glomerules of amphibole and biotite in the enclave. **h** Columnar and acicular apatite. *MME* microgranular enclave, *Apt* apatite, *Kfs* K-feldspar

Excimer laser-ablation system. The detailed operating conditions and data reduction procedures follow those described in Geng et al. (2017) and Yu et al. (2020a), and are listed in Table A.1 in the format proposed by Horstwood et al. (2016). Zircon and apatite analyses were conducted with a beam diameter of 30 and 40 µm respectively and an 8 Hz repetition rate. Each analysis incorporated a background acquisition of 20 s (gas blank) followed by data acquisition from the sample. Off-line selection and integration of background and analyte signals, and time-drift correction and quantitative

Table 1 Summary of sample information

No	Location	Lithology	Texture	Mineral assemblage	Analytical contents
17DM06	Damai stock, 102° 42′ 02″ E, 35° 13′ 28″ N, 2760 m	Granodiorite	Fine- to medium -grained hypidiomorphic-granular	Qz (35%), Pl (35%), Bt (15%), Amp (10%), and Kfs (5%)	Zircon U–Pb; Zircon Raman
17MR02	Meiwu batholith, 103° 10′ 39″ E, 35° 03′ 38″ N, 3560 m	Granodiorite	Medium -grained hypidiomorphic-granular	Pl (40%), Qz (30%), Kfs (15%), Bt (10%), and Amp (5%)	Zircon U–Pb; Zircon Raman; Apatite U–Pb and trace element; TEM; Biotite EPMA
17MR16	Meiwu batholith, 103° 10′ 39″ E, 35° 03′ 38″ N, 3560 m	Microgranular enclave	Fine-grained hypidiomorphic-granular	Bt (35%), Amp (25%), Pl (25%), and Qz (15%)	Zircon U–Pb; Zircon Raman; Apatite U–Pb and trace element; Biotite EPMA

calibration for U–Pb dating were performed using in-house software ICPMSDataCal 11.8 (Liu et al. 2010). Standard bracketing and linear fitting of adjacent standards are applied to correct the isotopic fractionation. Uncertainty propagated from external standard are also performed by the software (Liu et al. 2010). Plešovice zircon (primary; weighted mean ^{206}Pb/^{238}U date at 336.9 ± 1.88 Ma; Sláma et al. 2008) and 91500 zircon (secondary; weighted mean ^{206}Pb/^{238}U date at 1064.0 ± 5.6 Ma; Wiedenbeck et al. 1995) were used as the age reference materials for zircon U–Pb geochronology analyses. Plešovice zircon (primary; weighted mean ^{206}Pb/^{238}U date at 336.6 ± 3.4 Ma; Sláma et al. 2008), Otter Lake apatite (primary; Tera–Wasserburg concordia lower intercept date at 911 ± 48 Ma; Barfod et al. 2005) and MAD2 apatite (secondary; Tera–Wasserburg concordia lower intercept date at 476.2 ± 7.8 Ma; Cochrane et al. 2014) were used as the age reference materials for apatite U–Pb geochronology analyses. The NIST SRM 610 and 612 reference material glasses were used as an external standard to calculate U, Th, and Pb concentrations of zircon and apatite, respectively. The internal element standard isotope was ^{43}Ca for apatite trace element analyses. The typical analytical uncertainty ranges from 10% for light rare earth elements (LREE) to 5% for other trace elements. Zircon U–Pb data were not corrected for common Pb. Common Pb correction of apatite U–Pb data employed a Tera–Wasserburg Concordia approach, which involved projecting a straight line through the uncorrected data on a Tera–Wasserburg Concordia to determine the common Pb-component on the ^{207}Pb/^{206}Pb axis and the ^{238}U/^{206}Pb age can then be calculated as a lower intercept ^{238}U/^{206}Pb age on the concordia (Chew et al. 2014). Age calculations and concordia plots were reported at the 2σ uncertainty level and were processed using the Isoplot software (version 3.75; Ludwig 2012).

Zircon radiation damage calculations

The degree of radiation damage is quantitatively described as a time-integrated α-fluence (Dα) and is estimated using U and Th contents, and the apparent age (Ewing et al. 2003; Gao et al. 2014). Following Ewing et al. (2003), Dα is calculated by the following formula:

$$D\alpha = 8 * N_{238}[\exp(t/\tau_{238} - 1)] + 7 * N_{235}\left[\exp(t/\tau_{235} - 1)\right] + 6 * N_{232}\left[\exp(t/\tau_{232} - 1)\right], \quad (1)$$

where N_{238}, N_{235}, and N_{232} are the numbers of atoms/g of ^{238}U, ^{235}U and ^{232}Th; τ_{238}, τ_{235}, and τ_{232} are the half-lives of ^{238}U, ^{235}U and ^{232}Th and t is the apparent age (Ewing et al. 2003; Gao et al. 2014).

Raman spectroscopy

Raman spectra were collected to determine the relationship between crystal structure, Dα, and ^{206}Pb/^{238}U apparent age. Raman micro-analysis was performed using the JY Horiba LabRam HR Evolution microprobe with a 532 nm Ar laser excitation at the Analytical Laboratory of the Beijing Research Institute of Uranium Geology, Beijing, China. Spectra were acquired at room temperature using a 2 μm laser beam. The Raman spot was placed in the same textural zones identified by CL-imaging, and immediately adjacent to the ablation pit created by the LA–MC–ICPMS measurement, facilitating comparison against a known Dα (White and Ireland 2012; Gao et al. 2014). The full width at half-maximum of the $\nu_3(SiO_4)$ Raman band at ~1000 cm^{-1} (FWHMν_3) was calculated by band fits assuming Gaussian shapes using the *ORIGIN 2018* software.

Transmission electron microscopy

Zircon grain of 17MR02.1 was selected for focused ion beam (FIB) sampling at the Center for Lunar and Planetary Sciences, Institute of Geochemistry, Chinese Academy of Sciences. The ion-milled and thinned sample was analyzed using a TEM FEI Talos F200S, operating at 200 kV at the CAS Key Laboratory of Mineralogy and Metallogeny and Guangdong Provincial Key Laboratory of Mineral Physics

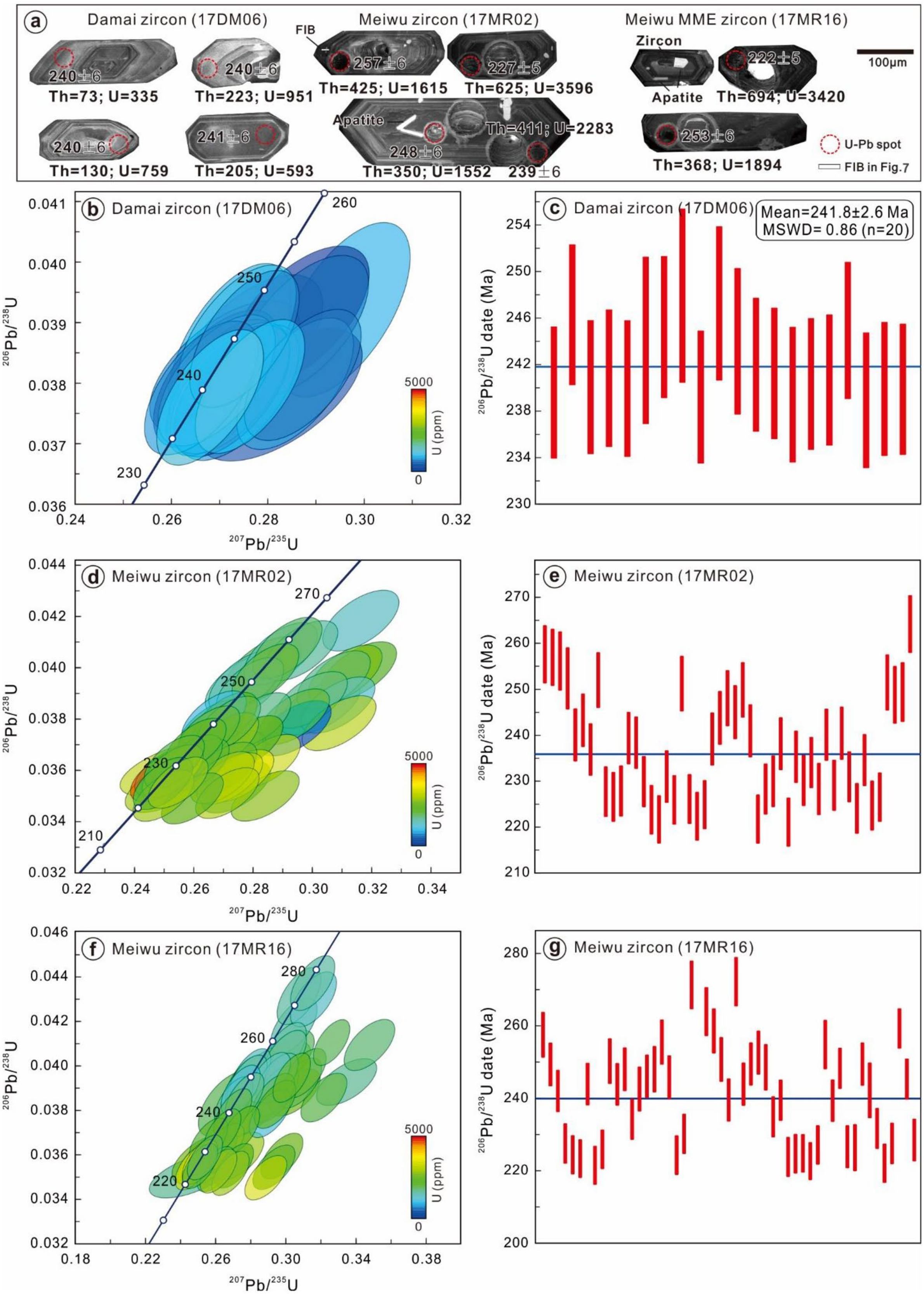
a
Damai zircon (17DM06)
240±6
Th=73; U=335
240±6
Th=223; U=951
240±6
Th=130; U=759
241±6
Th=205; U=593
Meiwu zircon (17MR02)
FIB
257±6
Th=425; U=1615
227±5
Th=625; U=3596
Apatite
248±6
Th=350; U=1552
Th=411; U=2283
239±6
Meiwu MME zircon (17MR16)
Zircon
Apatite
222±5
Th=694; U=3420
253±6
Th=368; U=1894
100μm
U-Pb spot
FIB in Fig.7
b Damai zircon (17DM06)
$^{206}Pb/^{238}U$
$^{207}Pb/^{235}U$
0.036
0.037
0.038
0.039
0.040
0.041
0.24
0.26
0.28
0.30
0.32
230
240
250
260
5000
U (ppm)
0
c Damai zircon (17DM06)
Mean=241.8±2.6 Ma
MSWD= 0.86 (n=20)
$^{206}Pb/^{238}U$ date (Ma)
230
234
238
242
246
250
254
d Meiwu zircon (17MR02)
$^{206}Pb/^{238}U$
$^{207}Pb/^{235}U$
0.032
0.034
0.036
0.038
0.040
0.042
0.044
0.22
0.24
0.26
0.28
0.30
0.32
0.34
210
230
250
270
5000
U (ppm)
0
e Meiwu zircon (17MR02)
$^{206}Pb/^{238}U$ date (Ma)
210
220
230
240
250
260
270
f Meiwu zircon (17MR16)
$^{206}Pb/^{238}U$
$^{207}Pb/^{235}U$
0.032
0.034
0.036
0.038
0.040
0.042
0.044
0.046
0.18
0.22
0.26
0.30
0.34
0.38
220
240
260
280
5000
U (ppm)
0
g Meiwu zircon (17MR16)
$^{206}Pb/^{238}U$ date (Ma)
200
220
240
260
280

◂**Fig. 4** **a** CL images showing variable morphologies and internal textures in zircon separated from Damai and Meiwu samples. **b**, **c** Wetherill concordia and $^{206}Pb/^{238}U$ age plots for zircon U–Pb analyses of the *Damai granodiorite* (17DM06). The weighted mean date represents the crystallization age of the *Damai granodiorite*. **d**–**g** Wetherill concordia and 206Pb/238U age plots for zircon U–Pb analyses of *Meiwu granodiorite* (17MR02) and microgranular enclave (17MR16). Wide range of zircon $^{206}Pb/^{238}U$ dates could be attributed to metamictization caused by radiation damage. Data-point error ellipses and bars are at the 2σ uncertainty level

and Materials, Guangzhou Institute of Geochemistry, Chinese Academy of Sciences. The detailed operating conditions and data reduction follow that previously described in Gu et al. (2018), Xu et al. (2018) and Xian et al. (2019).

The FIB milling was conducted with a Zeiss Auriga Compact dual beam instrument equipped with an Omniprobe AutoProbe 200 micromanipulator. Ion beam conditions for the final thinning and polishing were 5–30 kV high voltage with beam currents of 43 pA–5 nA. The FIB sections were prepared to ~100 nm thickness and ~10×3 μm^2 in area. Phase structures were analyzed by high resolution TEM imaging (HRTEM) and selected area electron diffraction (SAED).

Electron probe micro-analysis of biotite

The major element compositions of biotite in thin section from the *Meiwu granodiorite* (17MR02) and MME (17MR16) was undertaken using a JXA-8230 electron-probe micro-analyser at the Analytical Laboratory of the Beijing Research Institute of Uranium Geology, Beijing, China. The instrument was operated with an accelerating voltage of 15 kV, a probe current of 20 nA, and a 5 μm focused electron beam size. Detailed operating conditions, calibration standards, and data correction follow those described in Qiu et al. (2019). The crystallo-chemical formulae were calculated on the basis of 22 oxygens.

Biotite geothermobarometer

The Al and Ti contents of biotite in granitoids may be used to estimate the crystallization pressure and temperature. The crystallization pressure of biotite was estimated as follows (Uchida et al. 2007):

$$\mathrm{P\ (kbar)} = 3.03 \times \mathrm{Al}^{\mathrm{T}} - 6.53(\pm 0.33), \quad (2)$$

where Al$^{\mathrm{T}}$ is the number of atom per formula unit (apfu) normalized on the basis of 22 oxygens. Crystallization temperature of biotite is expressed as follows (Henry et al. 2005):

$$T\,(^{\circ}\mathrm{C}) = \left(\left(\ln(\mathrm{Ti}) - a - c \times \left(X_{\mathrm{Mg}}\right)^{3}\right)/b\right)^{0.33} (\pm 12^{\circ}\mathrm{C}), \quad (3)$$

where Ti is the number of apfu, the X_{Mg} is Mg/(Mg + Fe), $a = -2.3594$, $b = 4.6482 \times 10^{-9}$, and $c = 1.7283$. The application conditions for this biotite geothermometer are Ti (apfu) = 0.04–0.60, $X_{\mathrm{Mg}} = 0.275$–1.000, and $T = 480$–800 °C (Henry et al. 2005).

Analytical results

Zircon morphology and LA–MC–ICPMS U–Pb ages

Zircon crystals separated from Damai and Meiwu samples show variable morphologies and internal textures in CL images (Fig. 4a). Most zircon grains from *Damai granodiorite* (17DM06) are pristine, euhedral and display well-developed oscillatory, lengthwise, and sector growth zoning (Fig. 4a). The crystals have lengths of 100–180 μm and aspect ratios of 2:1 to 3:1. Zircon crystals from *Meiwu granodiorite* (17MR02) and the microgranular enclave (17MR16) are euhedral, exhibit low CL responses, but show oscillatory growth zoning (Fig. 4a). They vary from 110 to 220 μm in length, with aspect ratios between 2:1 and 3:1. Fine-grained mineral inclusions are visible in most crystals in CL images from the *Meiwu granodiorite* and microgranular enclave samples. Most of the inclusions are zircon and apatite, and a few are feldspar and thorite (Fig. 4a).

The results of the LA–MC–ICPMS zircon U–Pb dating are presented in Table A.2 and illustrated in Fig. 4. The age of the *Damai granodiorite* is determined by 20 dates from 20 grains from sample 17DM06, yielding a weighted mean $^{206}Pb/^{238}U$ date of 241.8 ± 2.6 Ma (2σ) (MSWD = 0.86) (Fig. 4c). They show Th and U contents of 42–307 ppm and 196 to 1101 ppm respectively. The Th/U ratios range from 0.14 to 0.36, most of which are between 0.20 and 0.35 (Table A.1; Fig. 4b).

Sixty-two analyses on 61 grains were undertaken on *Meiwu granodiorite* (17MR02). Twelve analyses yielded large discordance (>15%) and are excluded from age calculations (Table A.2). The measured Th and U contents of the remaining 49 analyses ranges from 100 to 772 ppm and 193 to 4876 ppm, with Th/U ratios ranging from 0.10 to 0.52 (Table A.2; Fig. 4d). They yield disturbed $^{206}Pb/^{238}U$ dates ranging between 221 and 264 Ma (Fig. 4e). Of the 96 analyses on 94 zircon grains from the *Meiwu microgranular* enclave (17MR16), 44 analyses recorded significant discordance (>15%) and one zircon is inherited in origin ($^{207}Pb/^{206}Pb$ age of 1833 Ma) and is omitted from the age calculations. The remaining 51 spots yield 181–738 ppm Th, 1009–3688 ppm U, Th/U ratios of 0.10 to 0.30 and show significant disturbance of the U-Pb isotope system (Fig. 4f). They have highly scattered $^{206}Pb/^{238}U$ dates ranging from 222 to 276 Ma (Fig. 4g).

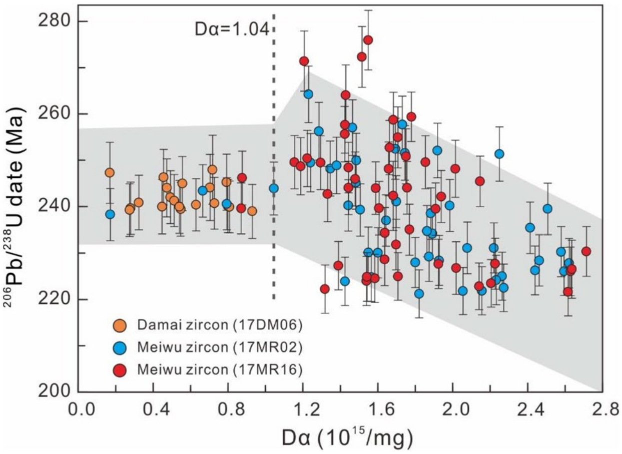

Fig. 5 ^{206}Pb/^{238}U ages versus Dα for zircon U–Pb analyses of the *Damai granodiorite* (17DM06) and *Meiwu granodiorite* (17MR02) and microgranular enclave (17MR16). Data-point error bars are at the 2σ uncertainty level

Zircon Dα values

The Dα values of zircon that crystallized in the granodiorites and the microgranular enclave are presented in Table A.3 and illustrated in Fig. 5. The Damai zircon crystals (17DM06) yield Dα values at 0.17 to 0.93 (10^{15}/mg), with a mean value of 0.56 (10^{15}/mg). The *Meiwu granodiorite* (17MR02) zircon crystals show high Dα values, ranging from 0.17 to 3.80 (10^{15}/mg), with a mean value of 1.83 (10^{15}/mg). The 51 zircon crystals from Meiwu microgranular enclave (17MR16) exhibit high Dα values, ranging from 0.87 to 2.87 (10^{15}/mg), with a mean value of 1.71 (10^{15}/mg) (Table A.3; Fig. 5).

Zircon Raman spectra

Following the LA–ICPMS U–Pb dating, Raman spectra of magmatic zircon crystals were measured. The results of the Raman analyses are shown in Fig. 6. Seven dominant peaks occur at ca. 205, 212, 220, 353, 437, 973, and 1004 cm^{-1} with the most intense peak being 1004 cm^{-1} in the majority

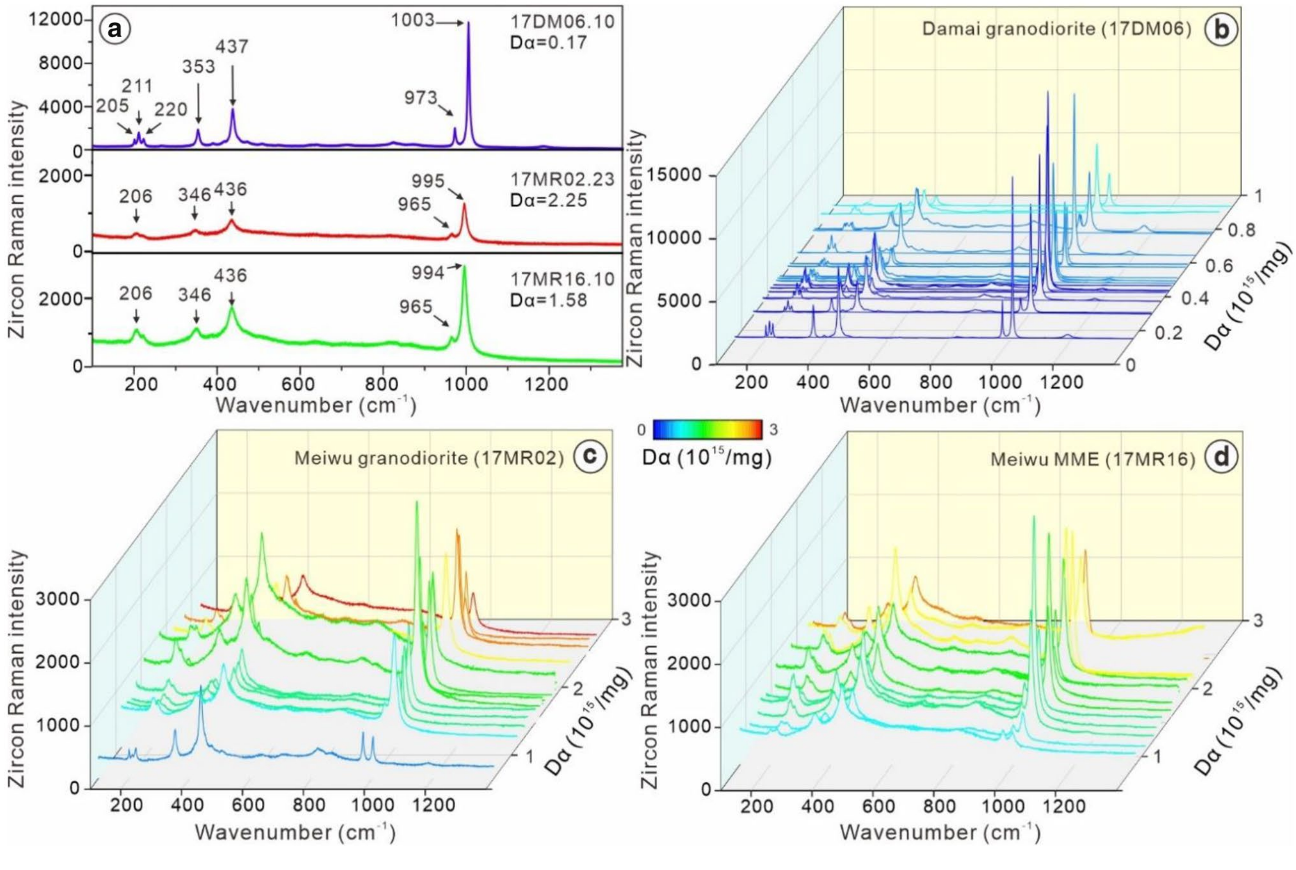

Fig. 6 **a** Representative Raman spectra of the *Damai granodiorite* (17DM06) and *Meiwu granodiorite* (17MR02) and microgranular enclave (17MR16). **b–d** Raman spectra versus Dα of the Damai and Meiwu zircon. Compared with distinct, narrow internal and external vibrational modes in Raman spectra of the Damai zircon, the Raman bands from Meiwu decrease in intensity, increase in half-width height, and show a notable shift towards lower wavenumbers

of the zircon crystals from the *Damai granodiorite* (Table A.3; Fig. 6a, b). However, the spectral bands for the zircon crystals from the *Meiwu granodiorite* and enclave are broader, with some peaks disappearing completely. Generally, five dominant peaks occur at ca. 206 (covering two adjacent peaks), 346, 436, 965, and 995 cm^{-1} and sometimes the 965 peak is covered by the broader 995 cm^{-1} peak (Table A.3; Fig. 6a, c, d). Of the bands representing internal vibrations of SiO_4 tetrahedra, the $v_3(SiO_4)$ Raman band (frequency about 1000 cm^{-1}) is the most sensitive and its intensity becomes weaker in the zircon from the *Meiwu granodiorite* and enclave.

Zircon and apatite transmission electron microscopy

Detailed examination by TEM of foils taken from Meiwu zircon (17MR02.1) (see Fig. 4a for location) reveals that the grain contains banded damaged zones (Fig. 7). The zones are a few hundred nanometers wide and parallel to the oscillatory zoning (Fig. 7a, b). The crystalline zircon shows an almost perfect crystalline structure (Fig. 7c), while HRTEM and SAED images of the damaged zones show amorphous domains (Fig. 7d, e). The apatite inclusion shows a perfectly crystalline structure (Fig. 7f).

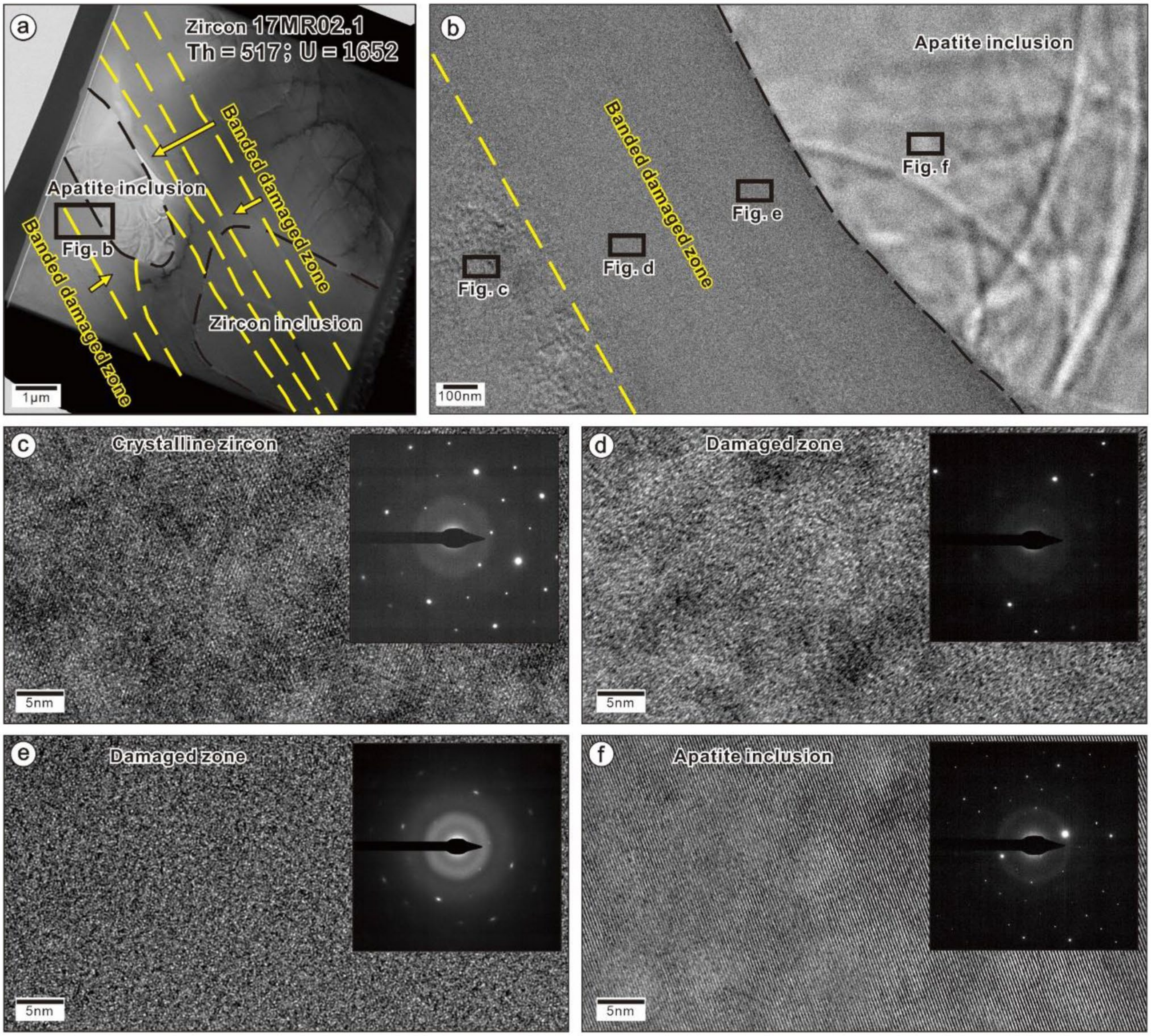

Fig. 7 **a**, **b** TEM images showing banded damaged zone in zircon. **c**–**f** HRTEM images of crystalline zircon, damaged zircon, damaged zircon, and crystalline apatite with insets of the SAED

Apatite morphology, composition and LA–ICPMS U–Pb dating

Apatite crystals separated from *Meiwu granodiorite* (17MR02) are pristine and euhedral without obvious fractures and inclusions. They vary from 80 to 200 μm in length, with aspect ratios between 2 and 3. The crystals are dark in CL images and display fine oscillatory growth zoning (Fig. 8a). Thirty-one analyses on 31 grains define a well-constrained mixing line between the radiogenic and the common Pb components, yielding a U–Pb Tera–Wasserburg concordia lower intercept date of 240.4 ± 3.8 Ma with an MSWD = 1.0 (2*σ*) (Table A.4; Fig. 8a). The lower intercept was anchored using a ^{207}Pb/^{206}Pb value of 0.852 derived from the Stacey and Kramers (1975) terrestrial Pb evolution model. The Tera–Wasserburg U–Pb unanchored lower intercept date is 240.4 ± 8.0 Ma with an MSWD = 1.0 (2*σ*). The apatite crystals have Th contents of 9–235 ppm, U contents of 14–235 ppm, with Th/U ratios of 0.27–1.22. Apatite crystals from the Meiwu microgranular enclave (17MR16) are anhedral and pristine without obvious fractures and inclusions. All grains are between 80 and 120 μm in size, with elongation ratios ranging between 1 and 1.5. These apatite crystals are CL bright and display faint zoning patterns (Fig. 8b). Twenty-nine analyses on 29 grains yielded a U–Pb Tera–Wasserburg concordia lower intercept date of 239.9 ± 4.0 Ma (2σ) with an MSWD of 2.1. The lower intercept was anchored using a ^{207}Pb/^{206}Pb value of 0.852 (Stacey and Kramers 1975). The Tera–Wasserburg U–Pb unanchored lower intercept date is 240.0 ± 10.8 Ma with an MSWD = 2.1 (2σ). They have Th content of 35–139 ppm, U content of 23–191 ppm, with Th/U ratios ranging from 0.38 to 1.74 (Table A.2; Fig. 8b).

Most of the apatite crystals from the *Meiwu granodiorite* (17MR02) yield relatively uniform abundances on trace element plots (Fig. 9a), except for two analyses 17MR02.19 and 17MR02.22. The rest of them have Sr contents ranging from 161 to 271 ppm, Y contents ranging from 854 to 3976 ppm, and Sr/Y ratios from 0.04 to 0.32 (Table A.5). The chondrite normalized values show slight enrichment in the LREE (mean LREE/HREE = 2.79), no Ce anomaly (mean Ce/Ce* = 1.19), and

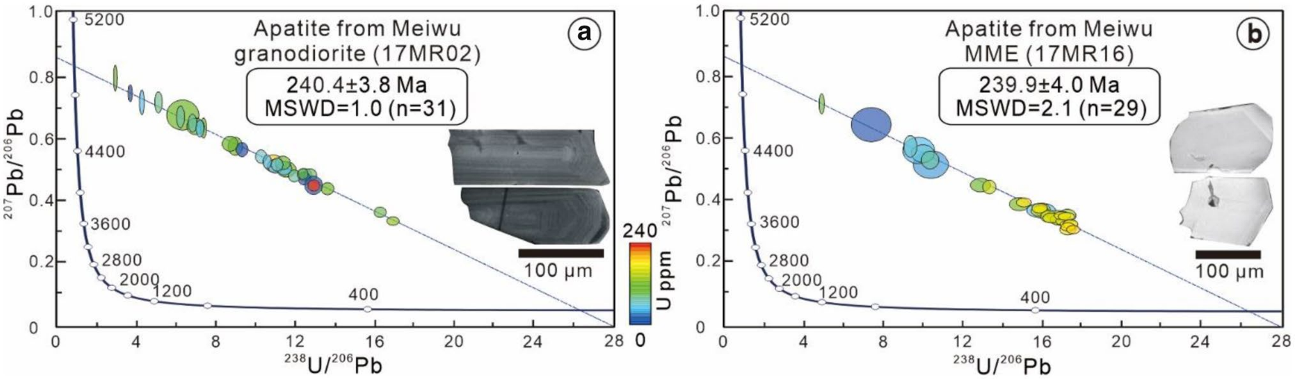

Fig. 8 Tera-Wasserburg concordia plots for apatite U–Pb analyses of the *Meiwu granodiorite* (17MR02, **a**) and microgranular enclave (17MR16, **b**), representing their crystallization ages. Data-point error ellipses are 2*σ* uncertainty level

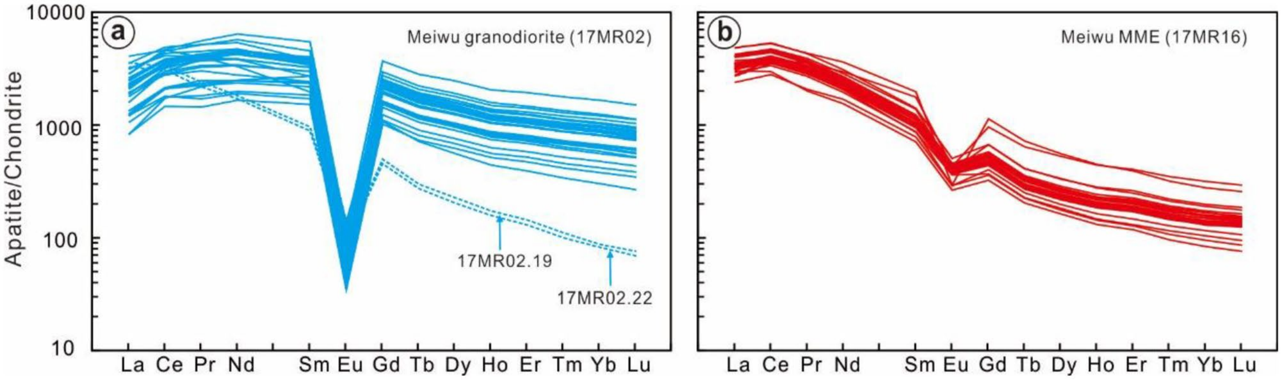

Fig. 9 Chondrite-normalized rare earth element patterns for apatite of the *Meiwu granodiorite* (17MR02, **a**) and microgranular enclave (17MR16, **b**). The REE concentrations are normalized to the chondrite composition reported by McDonough and Sun (1995)

a pronounced negative Eu anomaly (mean Eu/Eu* = 0.03) (Fig. 10a). The apatite crystals from Meiwu microgranular enclave (17MR16) also exhibit a minimal scatter in the trace element compositions (Fig. 9b). They have Sr contents ranging from 677 to 975 ppm, Y contents ranging from 221 to 863 ppm, with Sr/Y ratios from 0.79 to 4.41 (Table A.3). Plots of chondrite normalized REE values are characterized by distinct enrichment in the LREE (average of LREE/HREE = 18.79), no Ce anomaly (mean Ce/Ce* = 1.18), and a negative Eu anomaly (mean Eu/Eu* = 0.54) (Fig. 10b).

Biotite composition and estimations of crystallization pressure and temperature

The EPMA results of biotite grains are presented in the Table A.6. Biotite grains from the Meiwu granite (17MR02) and MME (17MR16) have similar major element compositions. The Meiwu granite biotite yields SiO_2 of 37.17–38.46%, MgO of 11.94–12.74%, Al_2O_3 of 13.96–14.46%, and TiO_2 of 2.87–3.35%. The Meiwu MME biotite has SiO_2 of 35.41–39.28%, MgO of 11.89–14.46%, Al_2O_3 of 13.55–15.05%, and TiO_2 of 2.94–3.55%. Crystallization pressures for granite range from 0.99 to 1.27 kbar, with an average at 1.08 ± 0.17 kbar, equivalent to a depth of 4.1 ± 0.6 km. The MME show similar crystallization pressures ranging from 0.73 to 1.50 kbar, with an average at 1.08 ± 0.17 kbar, equivalent to a depth of 4.1 ± 0.6 km. Crystallization temperatures for the granite vary from 694 to 710 °C, with a mean value of 697 ± 6 °C, similar to those for MME that vary from 703 to 725 °C, with a mean value of 712 ± 6 °C.

Discussion

Radiation damage of zircon from the Meiwu batholith

Zircon crystals from *Damai granodiorite* and *Meiwu granodiorite* and enclaves show oscillatory zoning or lengthwise zoning, all of which suggest a magmatic origin (Fig. 4a; Corfu et al. 2003; Yu et al. 2020a). The Damai zircon crystals yield $^{206}Pb/^{238}U$ dates ranging from 239 to 248 Ma and a weighted mean $^{206}Pb/^{238}U$ date at 241.9 ± 2.6 Ma, which is interpreted as the crystallization age for the intrusion (Fig. 4c). Compared with the Damai zircon crystals, the crystals from *Meiwu granodiorite* and enclaves yield a wide range of $^{206}Pb/^{238}U$ dates from 221 to 264 Ma and 222 to 276 Ma respectively (Fig. 4e, g). Generally, such a wide range of apparent zircon crystallization dates is unreasonable for a simple igneous crystallization history and could be attributed to metamictization caused by radiation damage (Nasdala et al. 2003; Kusiak et al. 2013; Gao et al. 2014; Spencer et al. 2016; Widmann et al. 2019; Deng et al. 2020a; Fu et al. 2021). The Raman spectra of Damai zircon grains are similar to those of non-metamict zircon, with distinct, narrow internal and external vibrational modes, indicating that the Damai zircon is crystalline (Fig. 6a, b; Nasdala et al. 2003). However, the $\nu_3(SiO_4)$ Raman bands for zircon from Meiwu decrease in intensity, increase in FWHM (~ 17 cm^{-1} for Meiwu compared to ~ 7 cm^{-1} for Damai), and show a notable shift towards lower wavenumbers compared with the Raman spectra of the Damai zircon (~ 996 cm^{-1} for Meiwu compared to ~ 1004 cm^{-1} for Damai) (Fig. 6). Such Raman spectra confirm that all the zircon from Meiwu are significantly more metamict (Nasdala et al. 2003). In addition, a banded texture is observed in TEM images of the Meiwu zircon (Fig. 7a). The mosaic texture shown by

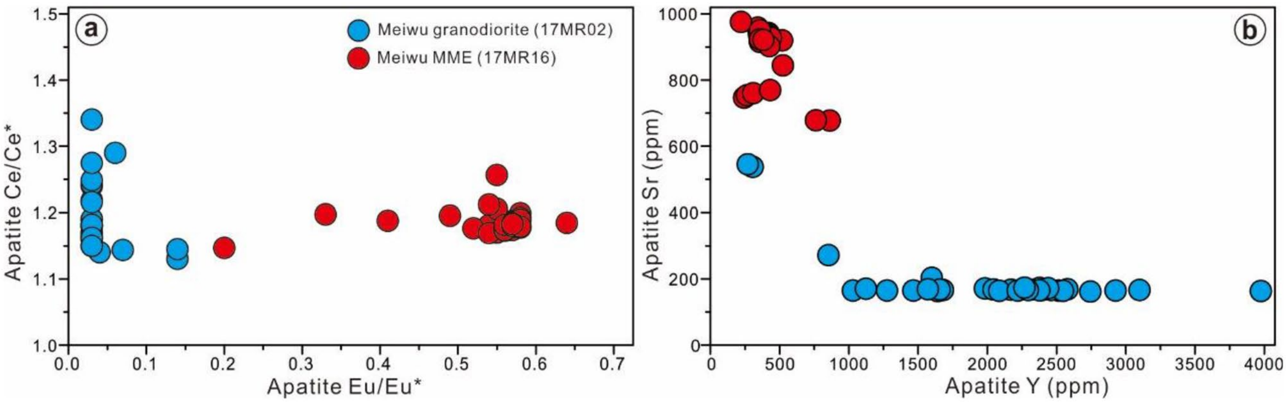

Fig. 10 Plots of Ce/Ce* versus Eu/Eu* (**a**) and Sr versus Y (**b**) for apatite of the *Meiwu granodiorite* (17MR02, **a**) and microgranular enclave (17MR16, **b**)

elliptical distortion of the diffraction spots indicates that damage accumulates along the oscillatory zoning, eventually creating banded damaged zones (Utsunomiya et al. 2004). HRTEM and SAED images show that the damaged zones near the mineral inclusions have the lowest crystallinity, suggesting that significant radiation damage takes place preferentially at the mineral interface (Fig. 7d, e).

Metamorphic zircon with an irregular redistribution of Pb due to mobilization of radiogenic Pb leading to spurious dates is commonly reported in zircon studies (Kusiak et al. 2015; Valley et al. 2015; Ge et al. 2019; Lyon et al. 2019). In some cases, the apparent zircon dates are much younger, which is attributed to either episodic Pb loss during later geological events or longer-term diffusive radiogenic Pb loss (e.g.,Kusiak et al. 2013; Peterman et al. 2016; Widmann et al. 2019). If Pb is mobilized within zircon grains, it accumulates and as a result causes either Pb clusters (Kusiak et al. 2013; Valley et al. 2015) or Pb nanospheres (Kusiak et al. 2015; Whitehouse et al. 2017; Lyon et al. 2019). The intra-crystalline radiogenic Pb accumulation would result in a high radiogenic Pb content in an analysis and therefore produce spurious isotopic ratios and old dates (e.g.,Utsunomiya et al. 2004; Valley et al. 2015; Peterman et al. 2016; Whitehouse et al. 2017; Ge et al. 2019). Our U–Pb results show that ^{206}Pb/^{238}U dates for zircon with D$\alpha > 1.04$ (10^{15}/mg) are disturbed, exhibiting not only much older dates, but also much younger dates than those with D$\alpha < 1.04$ (10^{15}/mg) (Fig. 5). It reinforces explicitly the idea that U–Pb dating of metamict zircon like those from Meiwu is commonly complicated by both apparent Pb loss and gain (Kusiak et al. 2015; Ge et al. 2019; Lyon et al. 2019; Widmann et al. 2019). Significantly, the ^{206}Pb/^{238}U date decreases as Dα increases (Fig. 5), implying that Pb loss is a more important control on disturbance of the zircon U–Pb age system in the Meiwu samples. As such, the radiation damage of zircon limits its accuracy as a geochronometer.

Apatite petrochronological constraints on the age of the Meiwu batholith

The apatite crystals from the *Meiwu granodiorite* and enclave yield U–Pb Tera–Wasserburg concordia lower intercept dates of 240.4 ± 3.8 and 239.9 ± 4.0 Ma, with MSWDs of 1.0 and 2.1 (Fig. 8). Whether these dates can represent crystallization ages for the Meiwu batholith needs to be estimated by the closure temperature for apatite U–Pb and cooling duration of the batholith (Zhang et al. 2010). Simulated and experimental results indicated the closure temperature for Pb diffusion in apatite has a wide range varying from 350 to 550 °C, and even up to 770 to 870 °C (Cherniak et al. 1991; Chew and Spikings 2015; Pochon et al. 2016). It is therefore necessary to estimate the closure temperature of the studied apatite crystals for evaluating the significance of the apatite U–Pb dates (Pochon et al. 2016). The Pb diffusion parameters were controlled by effective diffusive radius and cooling rate (Dodson 1973; Cherniak et al. 1991). The apatite crystals from the Meiwu batholith are typically > 100 microns in length (Fig. 8). The cooling rate is estimated at over 100 °C/Ma by Ar–Ar dates of coexisting amphibole (243.34 Ma) and biotite (244.05 Ma) (unpublished data). The apatite U–Pb closure temperature is thus calculated at 530 °C (Cherniak et al. 1991; Chamberlain and Bowring 2001). Zhang et al. (2010) proposed a mathematical model to constrain the cooling duration of the pluton on the basis of the geothermic model (Buntebarth 2012):

$$\mathrm{erf}\left(\frac{D}{2\sqrt{kt}}\right) = \sqrt[3]{\left(\frac{\mathrm{Tf}-\mathrm{Tw}}{\mathrm{Ti}-\mathrm{Tw}}\right)}, \tag{4}$$

where erf $(x) = (2/\sqrt{\pi})\int_0^x \exp\left(-t^2\right)dt$, D is the radius (km), k is the thermal diffusivity (10^{-3} cm^{2}s^{-1}), t is the cooling time (Ma), Tf is the cooling temperature of pluton (°C), Tw is the temperature of wall rock (°C), Ti is the initial temperature of pluton (°C). In this study, $D = 5$ km based on the sample location; k is 2.92 (Zhang et al. 2010); Tf is 530 °C; Tis of granodiorite and MME are 697 °C and 712 °C, Tw is calculated as 82 °C based on the paleo-surface temperature of 0 °C, the paleo-geothermal gradient of 20 °C/km, and the paleo-depth of 4.1 km. The cooling durations from the crystallization temperature to the apatite U–Pb closure temperature of the granodiorite and MME obtained following these calculations are both 1.6 Ma.

Given the high closure temperature (530 °C) and rapid modeled cooling duration (1.6 Ma), the U–Pb dates obtained on apatite can effectively be represented as the crystallization ages for the granodiorite and MME, although the semi-quantitative estimates bear large uncertainties and are indicative values only. These results confirm that the Meiwu batholith belongs to the main phase of magmatism (250–235 Ma), associated with subduction of the Paleo-Tethys ocean (Luo et al. 2015; Yu et al. 2020a). The data are reasonably precise (2%) considering the young date of the samples in part because of the relatively higher U content of the apatite from Meiwu (9–235 ppm, Table A.1) than typical apatite (c. 12.5 ppm; O'Sullivan et al. 2018). The radiation damage in zircon caused by the emission of α-particles from the decay chains of U and Th accumulates, disrupts the lattice, and eventually leads to disturbances of apparent ^{206}Pb/^{238}U dates (Fig. 5). By contrast, apatite crystals from Meiwu are not metamict as observed in TEM images (Fig. 7f). The lower U and Th contents along with annealing processes that heal radiation damage, result in apatite remaining crystallographically intact and less likely to lose or gain Pb (Engi 2017). Apatite with high U content thus offers a convenient alternative to dating igneous rocks hosting metamict zircon.

Apatite geochemistry constrains the contribution of magma mixing to skarn systems in the Paleo-Tethys belt

Arc magmas formed along convergent plate margins are driven to more evolved and hydrous compositions by fractional crystallization, assimilation, and melting in the lower crust (e.g., Nathwani et al. 2020). The evolved and hydrous arc magmas may result in the formation of economically valuable magmatic-hydrothermal ore deposits (Sillitoe 2005; Qiu et al. 2021b). Magma mixing processes are considered to play important roles in facilitating volatile accumulation and enrichment in ore-forming components (e.g., Qiu and Deng 2017; Deng et al. 2020b). However, unraveling the process of magma mixing using bulk-rock compositions alone can be challenging because of the crustal contamination processes (Richards 2011). In addition, loss of elements in zircon by diffusion and bulk dissolution may proceed rapidly in radiation damaged domains, which may make the trace elements of metamict zircon an unreliable petrogenetic tracer (Finch and Hanchar 2003). Microgranular enclaves are commonly distributed within dozens of granitoids in the Xiahe–Hezuo polymetallic district, such as the Meiwu, Damai, Dewulu, and Xiahe granitoids, which host the Dewulu, Gangyi and Nanban skarn Cu deposits, and the Meiren and Riduoma skarn Fe deposits (Fig. 1; Luo et al. 2015; Qiu and Deng 2017). A magma mixing origin for these enclaves is shown by the wide variety of morphologies and contact interfaces with their hosts (Figs. 2, 3). Felsic back-veins penetrate or rise into enclaves, indicating rapid crystallization and solidification of the enclaves as the high-temperature mafic melt entered the relatively low-temperature granitic magma (Fig. 2b–d, f). Abundant megacrysts of feldspar and quartz surrounded by fine-grained plagioclase, biotite, and hornblende within the enclaves may be the result of the mechanical transfer of crystals (Figs. 2f, 3e, f). The porphyritic texture of granodiorite near the enclaves (Fig. 3b) and acicular apatite in quartz within the enclaves (Fig. 3h) indicate quenching. Plagioclase showing corrosion and overgrowths and glomerules of amphibole and biotite in the enclaves further show intimate mixing (Luo et al. 2015; Qiu and Deng 2017). Qiu and Deng (2017) proposed that the enclaves in the Dewulu granitoids near Meiwu were derived from partial melting of enriched sub-continental lithospheric mantle. The melt with a relatively high oxidation state ($\Delta FMQ = +3.3$) plays an important role in forming the Xiahe–Hezuo skarn Cu system (Qiu and Deng 2017). To better understand the contribution of mixing with contemporaneous mafic melts, the apatite geochemistry in the *Meiwu granodiorite* and enclave is investigated.

The main substitution mechanisms involving REE in apatite are (Cao et al. 2012; Engi 2017):

$$REE^{3+} + Na^{+} = 2Ca^{2+}, \tag{5}$$

$$REE^{3+} + SiO_4^{4-} = Ca^{2+} + PO_4^{3-}. \tag{6}$$

These substitution mechanisms suggest that Eu^{3+} and Ce^{3+} should be incorporated preferentially into apatite relative to Eu^{2+} and Ce^{4+}, making apatite an indicator of oxygen fugacity. Although the apatite of the *Meiwu granodiorite* shows much stronger negative Eu anomalies (mean $Eu/Eu^* = 0.03$) than those in the enclave (mean $Eu/Eu^* = 0.56$), no Ce anomalies are found in either the granodiorite and enclave apatite (mean $Ce/Ce^* = 1.19$ and 1.19), indicating similar and low oxygen fugacity in the *Meiwu granodiorite* and enclave (Fig. 10a; Cao et al. 2012). The pronounced Eu anomalies are thus more likely influenced by the crystallization of feldspars (Belousova et al. 2001). The Sr content of apatite is independent of the oxidation state, and the much lower Sr of the granodiorite apatite (194 ppm) than that of the enclave apatite (893 ppm) also supports the crystallization of plagioclase in the granodiorite (Fig. 10b; Table A.3). Amphibole is known to concentrate HREE (Cao et al. 2012). By considering HREE abundances in amphibole, the data reveal that the enclave apatite with higher $(La/Yb)_N$ (23.58) are likely produced by earlier or coeval crystallization of amphibole, which is supported by the depletion in Y in the enclave apatite (407 ppm) (Fig. 10; Table A.3). As a result, the different REE patterns of the two types of apatite indicate the different crystallization sequence of amphibole and plagioclase in the granodiorite and enclave. Experimental petrology constraints have shown that the crystallization sequence of amphibole and plagioclase in arc magmas are influenced by water concentration, the total alkali content, temperature, and the oxidation state (Sisson and Grove 1993; Zimmer et al. 2010; Richards 2011; Loucks 2014; Scaillet et al. 2016; Tollan and Hermann 2019). Previous studies show that the *Meiwu granodiorite* and enclave share similar total alkali contents, ranging from 6.55 to 7.31 wt% and 6.24 to 7.68 wt% respectively (Luo et al. 2015). Ti-in-zircon thermometry implies the granodiorite crystallized at 672 °C and the enclave crystallized at a slightly higher temperature (759 °C) (Luo et al. 2015). Our apatite REE results and previous geochemical studies show that the granodiorite and enclave have a similar oxygen fugacity. Phase relationships of metaluminous silicic magmas indicate that H_2O destabilizes plagioclase and therefore increases the proportion of Fe–Mg silicates that crystallize early (Sisson and Grove 1993; Scaillet et al. 2016). Moreover, higher temperature requires higher water content to maintain amphibole stability (Scaillet et al. 2016). Amphibole and plagioclase fractionation from the *Meiwu granodiorite* and enclave therefore reflect variable water contents in arc magmas. Loucks (2014) pointed out that the crystallization sequence of silicates from dry melt is plagioclase, olivine orthopyroxene and then augite. However, when there is > 6.5 wt% H_2O dissolved in the melt amphibole would be the first of those silicates to crystallize and plagioclase would crystallize last (Loucks 2014). As a result, the fractional crystallization of plagioclase in granodiorite as reflected by the strong apatite Eu anomaly and the relatively high content of Sr suggests a dry melt, while the relative depletion in HREE confirms the enclave as a product of a water-rich melt, resulting in amphibole fractionation and the suppression of plagioclase crystallization (Richards 2011).

Our apatite composition data imply that the arc magmas at Meiwu are relatively reduced and may have rendered the magma infertile for later porphyry deposit formation. Richards and Şengör (2017) proposed that the Paleo-Tethys ocean basin anoxia suppressed arc magma fertility for porphyry Cu formation because the reduced seafloor materials that were subducted for extensive periods of time are unlikely to generate fertile arc magmatic systems and secondary reduction of otherwise oxidized arc magmas may occur during ascent through crust containing chemically reduced lithologies. Compared with porphyry deposits that require relatively oxidized and hydrous magmas to form (Richards 2011; Loucks 2014; He et al. 2016; Richards and Şengör 2017; Yu et al. 2019), large-scale metasomatic transfer plays a critical role in most economically important skarn deposits (Meinert et al. 2005; He et al. 2015; Gao et al. 2020). Isotopic investigations and fluid inclusion studies have demonstrated the importance of magmatic waters in the evolution of the skarns, particularly in the prograde skarn stage (Meinert et al. 2005; Chang and Meinert 2008; Li et al. 2019). Multiple episodic incursions of magmatic-hydrothermal fluids released from the granitoids are considered as a critical factor for controlling the formation of giant skarn deposits (He et al. 2016; Qiu and Deng 2017; Li et al. 2019). Previous works showed that the widespread reduced intrusions and their associated skarns in West Qinling were genetically related to the subduction of the Paleo-Tethys ocean (e.g., Sui et al. 2017; Li et al. 2019). The occurrence of contemporaneous enclaves in host granitoids in West Qinling suggests magma mixing in the Early Triassic. The fluid exsolution would take place during the ascent of the water-rich magmas and the resultant decrease of water solubility with decreasing pressure (He et al. 2016). We therefore conclude that although the low oxidation state may decrease the metal endowment and metal ratios in ores precipitated by the hydrothermal system, the high magmatic water contents resulted in the exsolution of an aqueous volatile phase and is the key to the formation of the skarn systems in the Paleo-Tethys belt.

Conclusions

In this study, metamict zircon with $D\alpha > 1.04$ (10^{15}/mg) yield highly disturbed $^{206}Pb/^{238}U$ dates and cannot provide reliable LA–ICPMS U–Pb ages. Radiation damage accumulates along zircon oscillatory zoning and forms nanoscale banded damaged zones. These nanoscale zones make it impossible to correct these dates effectively. By contrast, apatite coexisted with the metamict zircon do not become metamict and show near perfect crystalline structure under transmission electron microscopy. Apatite therefore is effective in tracing the evolution of magmatic hydrothermal systems containing metamict zircon. A case study of *Meiwu granodiorite* and its microgranular enclaves reveals that they are contemporaneous and were emplaced at ca. 240 Ma. Apatite compositions confirm that the mixing of the hydrous and dry magmas induced production of hydrothermal-fluids that were enriched in metals, which contributed to the formation of widespread skarns in West Qinling.

Supplementary Information The online version contains supplementary material available at https://doi.org/10.1007/s00410-021-01827-z.

Acknowledgements We thank Prof. Daniela Rubatto at Institut für Geologie Universität Bern Switzerland, Prof. Fernando Corfu at University of Oslo, Prof. Monika Kusiak at Polish Academy of Sciences, and Dr. Yu-Ya Gao and Dr. Jing-Zhao Dou at China Academy of Sciences for thoughtful discussions. Zhi-Bin Xiao and Jia-Run Tu at China Geological Survey, Lin-Fei Qiu at Beijing Research Institute of Uranium Geology and Jia-Xin Xi, Rui Li and Yuan-Jing Wen at Chinese Academy of Sciences provided instruction, advice, and assistance during U-Pb dating, Raman and TEM measurements. This research was financially supported by the National Natural Science Foundation of China (91962106, 42072087, 42111530124, 41702069), the Beijing Nova Program (Z201100006820097), CAS Key Laboratory of Mineralogy and Metallogeny (KLMM20190101), the State Key Laboratory of Ore Deposit Geochemistry (201704) and the 111 Project of the Ministry of Science and Technology (BP0719021). Yu, Huang, and Hetheringtion gratefully acknowledged the support of the Society of Economic Geologists Foundation and the Overseas Experts Exchange Project of China University of Geosciences.

References

Barfod GH, Krogstad EJ, Frei R, Albarède F (2005) Lu–Hf and PbSL geochronology of apatites from Proterozoic terranes: a first look at Lu–Hf isotopic closure in metamorphic apatite. Geochim Cosmochim Acta 69(7):1847–1859

Belousova E, Walters S, Griffin W, O'reilly S (2001) Trace–element signatures of apatites in granitoids from the Mt Isa Inlier, northwestern Queensland. Aust J Earth Sci 48(4):603–619

Buntebarth G (2012) Geothermics: an introduction. Springer Science & Business Media, Berlin

Cao M, Li G, Qin K, Seitmuratova EY, Liu Y (2012) Major and trace element characteristics of Apatites in Granitoids from Central Kazakhstan: implications for Petrogenesis and Mineralization. Resour Geol 62(1):63–83

Cao MJ, Evans NJ, Qin KZ, Danišík M, Li GM, McInnes BI (2019) Open apatite Sr isotopic system in low–temperature hydrous regimes. J Geophys Res Solid Earth 124(11):11192–11203

Chamberlain KR, Bowring SA (2001) Apatite–feldspar U-Pb thermochronometer: a reliable, mid-range (~ 450 °C), diffusion-controlled system. Chem Geol 172(1–2):173–200

Chang Z, Meinert LD (2008) The Empire Cu–Zn mine, Idaho: exploration implications of unusual skarn features related to high fluorine activity. Econ Geol 103(5):909–938

Cherniak DJ, Lanford WA, Ryerson F (1991) Lead diffusion in apatite and zircon using ion implantation and Rutherford backscattering techniques. Geochim Cosmochim Acta 55(6):1663–1673

Chew DM, Spikings RA (2015) Geochronology and thermochronology using apatite: time and temperature, lower crust to surface. Elements 11(3):189–194

Chew DM, Sylvester PJ, Tubrett MN (2011) U-Pb and Th–Pb dating of apatite by LA–ICPMS. Chem Geol 280(1–2):200–216

Chew DM, Petrus JA, Kamber BS (2014) U-Pb LA–ICPMS dating using accessory mineral standards with variable common Pb. Chem Geol 363:185–199

Cochrane R, Spikings RA, Chew D, Wotzlaw JF, Chiaradia M, Tyrrell S, Schaltegger U, Van der Lelij R (2014) High temperature (> 350 C) thermochronology and mechanisms of Pb loss in apatite. Geochim Cosmochim Acta 127:39–56

Corfu F, Hanchar JM, Hoskin PW, Kinny P (2003) Atlas of zircon textures. Rev Mineral Geochem 53(1):469–500

Deng J, Wang QF (2016) Gold mineralization in China: Metallogenic provinces, deposit types and tectonic framework. Gondwana Res 36:219–274

Deng J, Wang CM, Zi JW, Xia R, Li Q (2018) Constraining subduction-collision processes of the Paleo-Tethys along the Changning-Menglian Suture: new zircon U-Pb ages and Sr-Nd-Pb-Hf-O isotopes of the Lincang Batholith. Gondwana Res 62:75–92

Deng J, Qiu KF, Wang QF, Goldfarb RJ, Yang LQ, Zi JW, Geng JZ, Ma Y (2020a) In-situ dating of hydrothermal monazite and implications on the geodynamic controls of ore formation in the Jiaodong gold province. Eastern China Econ Geol 115(3):671–685

Deng J, Yang LQ, Groves DI, Zhang L, Qiu KF, Wang QF (2020b) An integrated mineral system model for the gold deposits of the giant Jiaodong province, eastern China. Earth Sci Rev 208:103274

Deng J, Wang QF, Gao L, He WY, Yang ZY, Zhang SH, Chang LJ, Li GJ, Sun X, Zhou DQ (2021) Differential crustal rotation and its control on giant ore clusters along the eastern margin of Tibet. Geology 49(4):428–432

Dodson H (1973) Closure temperature in cooling geochronological and petrological systems. Contrib Mineral Petrol 40(3):259–274

Dong Y, Santosh M (2016) Tectonic architecture and multiple orogeny of the Qinling Orogenic Belt, Central China. Gondwana Res 29(1):1–40

Dong Y, Genser J, Neubauer F, Zhang G, Liu X, Yang Z, Heberer B (2011a) U-Pb and 40Ar/39Ar geochronological constraints on the exhumation history of the North Qinling terrane, China. Gondwana Res 19(4):881–893

Dong Y, Zhang G, Neubauer F, Liu X, Genser J, Hauzenberger C (2011b) Tectonic evolution of the Qinling orogen, China: review and synthesis. J Asian Earth Sci 41(3):213–237

Dong Y, Yang Z, Liu X, Sun S, Li W, Cheng B, Zhang F, Zhang X, He D, Zhang G (2016) Mesozoic intracontinental orogeny in the Qinling Mountains, central China. Gondwana Res 30:144–158

Engi M (2017) Petrochronology based on REE-minerals: Monazite, Allanite, Xenotime. Apatite Rev Mineral Geochem 83(1):365–418

Ewing RC, Meldrum A, Wang L, Weber WJ, Corrales LR (2003) Radiation effects in zircon. Rev Mineral Geochem 53(1):387–425

Finch RJ, Hanchar JM (2003) Structure and chemistry of zircon and zircon-group minerals. Rev Mineral Geochem 53(1):1–25

Fu JN, Pirajno F, Yang F, Shivute E, Sun YZ, Ai N, Qiu KF (2021) Integration of zircon and apatite U-Pb geochronology and geochemical mapping of the Wude basalts (Emeishan large igneous province): a tool for a better understanding of the tectonothermal and geodynamic evolution of the Emeishan LIP. Geosci Front 12(2):573–585

Gao YY, Li XH, Griffin WL, O'Reilly SY, Wang YF (2014) Screening criteria for reliable U-Pb geochronology and oxygen isotope analysis in uranium-rich zircons: a case study from the Suzhou A-type granites, SE China. Lithos 192–195:180–191

Gao X, Yang LQ, Yan H, Meng JY (2020) Ore-forming processes and mechanisms of the Hongshan skarn Cu–Mo deposit, Southwest China: Insights from mineral chemistry, fluid inclusions, and stable isotopes. Ore Energy Resour Geol 4:100007

Ge R, Wilde SA, Nemchin AA, Whitehouse MJ, Bellucci JJ, Erickson TM (2019) Mechanisms and consequences of intra-crystalline enrichment of ancient radiogenic Pb in detrital Hadean zircons from the Jack Hills, Western Australia. Earth Planet Sci Lett 517:38–49

Geng JZ, Qiu KF, Gou ZY, Yu HC (2017) Tectonic regime switchover of Triassic Western Qinling Orogen: Constraints from LA-ICP-MS zircon U-Pb geochronology and Lu–Hf isotope of Dangchuan intrusive complex in Gansu, China. Geochemistry 77(4):637–651

Gray AL (1985) Solid sample introduction by laser ablation for inductively coupled plasma source mass spectrometry. Analyst 110(5):551–556

Gregory CJ, McFarlane CRM, Hermann J, Rubatto D (2009) Tracing the evolution of calc-alkaline magmas: in-situ Sm–Nd isotope studies of accessory minerals in the Bergell Igneous Complex. Italy Chem Geol 260(1–2):73–86

Gu L, Zhang B, Hu S, Noguchi T, Hidaka H, Lin Y (2018) The discovery of silicon oxide nanoparticles in space-weathered of Apollo 15 lunar soil grains. Icarus 303:47–52

He WY, Mo XX, He ZH, White NC, Chen JB, Yang KH, Wang R, Yu XH, Dong GC, Huang XF (2015) The geology and mineralogy of the Beiya skarn gold deposit in Yunnan, southwest China. Econ Geol 110(6):1625–1641

He WY, Mo XX, Yang LQ, Xing YL, Dong GC, Yang Z, Gao X, Bao XS (2016) Origin of the Eocene porphyries and mafic microgranular enclaves from the Beiya porphyry Au polymetallic deposit, western Yunnan, China: implications for magma mixing/mingling and mineralization. Gondwana Res 40:230–248

Henry DJ, Guidotti CV, Thomson JA (2005) The Ti-saturation surface for low-to-medium pressure metapelitic biotites: implications for geothermometry and Ti-substitution mechanisms. Am Mineral 90(2–3):316–328

Horstwood MSA, Košler J, Gehrels G, Jackson SE, McLean NM, Paton C, Pearson NJ, Sircombe K, Sylvester P, Vermeesch P, Bowring JF, Condon DJ, Schoene B (2016) Community-derived standards for LA-ICP-MS U-(Th-)Pb geochronology—uncertainty propagation, age interpretation and data reporting. Geostand Geoanal Res 40(3):311–332

Hu H, Li JW, Harlov DE, Lentz DR, McFarlane CR, Yang YH (2020) A genetic link between iron oxide-apatite and iron skarn mineralization in the Jinniu volcanic basin, Daye district, eastern China: evidence from magnetite geochemistry and multi-mineral U-Pb geochronology. Bulletin 132(5–6):899–917

Hughes JM, Harlov D, Rakovan JF (2018) Structural variations along the apatite F-OH join. Am Mineral 103(12):1981–1987

Jt S, Kramers J (1975) Approximation of terrestrial lead isotope evolution by a two-stage model. Earth Planet Sci Lett 26(2):207–221

Kirkland CL, Yakymchuk C, Szilas K, Evans N, Hollis J, McDonald B, Gardiner NJ (2018) Apatite: a U-Pb thermochronometer or geochronometer? Lithos 318–319:143–157

Kogawa M, Watson EB, Ewing RC, Utsunomiya S (2012) Lead in zircon at the atomic scale. Am Mineral 97(7):1094–1102

Konecke BA, Fiege A, Simon AC, Linsler S, Holtz F (2019) An experimental calibration of a sulfur-in-apatite oxybarometer for mafic systems. Geochim Cosmochim Acta 265:242–258

Kusiak MA, Whitehouse MJ, Wilde SA, Nemchin AA, Clark C (2013) Mobilization of radiogenic Pb in zircon revealed by ion imaging: Implications for early Earth geochronology. Geology 41(3):291–294

Kusiak MA, Dunkley DJ, Wirth R, Whitehouse MJ, Wilde SA, Marquardt K (2015) Metallic lead nanospheres discovered in ancient zircons. Proc Natl Acad Sci 112(16):4958–4963

Li Q (2016) High-U effect during SIMS Zircon U-Pb dating. Bull Mineral Petrol Geochem 35(3):405–412

Li XW, Mo XX, Huang XF, Dong GC, Yu XH, Luo MF, Liu YB (2015) U-Pb zircon geochronology, geochemical and Sr–Nd–Hf isotopic compositions of the Early Indosinian Tongren Pluton in West Qinling: petrogenesis and geodynamic implications. J Asian Earth Sci 97:38–50

Li W, Xie GQ, Mao JW, Zhu QQ, Zheng JH (2019) Mineralogy, fluid inclusion, and stable isotope studies of the Chengchao deposit, Hubei province, eastern China: Implications for the formation of high-grade Fe skarn deposits. Econ Geol 114(2):325–352

Liu Y, Gao S, Hu Z, Gao C, Zong K, Wang D (2010) Continental and oceanic crust recycling-induced melt–peridotite interactions in the Trans-North China Orogen: U-Pb dating, Hf isotopes and trace elements in zircons from mantle xenoliths. J Petrol 51(1–2):537–571

Loucks R (2014) Distinctive composition of copper-ore-forming arc-magmas. Aust J Earth Sci 61(1):5–16

Ludwig K (2012) Isoplot 3.75. A Geochronological toolkit for Microsoft Excel. Berkeley Geochronology Center, Spec. Pub. 5

Luo BJ, Zhang HF, Xu W, Guo L, Pan FB, Yang H (2015) The Middle Triassic Meiwu Batholith, West Qinling, Central China: implications for the evolution of compositional diversity in a composite Batholith. J Petrol 56(6):1139–1172

Lyon IC, Kusiak MA, Wirth R, Whitehouse MJ, Dunkley DJ, Wilde SA, Schaumloffel D, Malherbe J, Moore KL (2019) Pb nanospheres in ancient zircon yield model ages for zircon formation and Pb mobilization. Sci Rep 9(1):13702

Mao M, Rukhlov AS, Rowins SM, Spence J, Coogan LA (2016) Apatite trace element compositions: a robust new tool for mineral exploration. Econ Geol 111(5):1187–1222

McDonough WF, Sun SS (1995) The composition of the Earth. Chem Geol 120(3–4):223–253

Meinert LD, Dipple GM, Nicolescu S (2005) World Skarn Deposits. Economic Geology 100th Anniversary Volume, pp 299–336

Nasdala L, Zhang M, Kempe U, Panczer G, Gaft M, Andrut M, Plötze M (2003) Spectroscopic methods applied to zircon. Rev Mineral Geochem 53(1):427–467

Nasdala L, Reiners PW, Garver JI, Kennedy AK, Stern RA, Balan E, Wirth R (2004) Incomplete retention of radiation damage in zircon from Sri Lanka. Am Mineral 89(1):219–231

Nathwani CL, Loader MA, Wilkinson JJ, Buret Y, Sievwright RH, Hollings P (2020) Multi-stage arc magma evolution recorded by apatite in volcanic rocks. Geology 48(4):323–327

O'Sullivan G, Chew D, Morton A, Mark C, Henrichs I (2018) An integrated apatite geochronology and geochemistry tool for sedimentary provenance analysis. Geochem Geophys Geosyst 19(4):1309–1326

Peterman EM, Reddy SM, Saxey DW, Snoeyenbos DR, Rickard WD, Fougerouse D, Kylander-Clark AR (2016) Nanogeochronology of discordant zircon measured by atom probe microscopy of Pb-enriched dislocation loops. Sci Adv 2(9):e1601318

Pochon A, Poujol M, Gloaguen E, Branquet Y, Cagnard F, Gumiaux C, Gapais D (2016) U-Pb LA-ICP-MS dating of apatite in mafic rocks: evidence for a major magmatic event at the Devonian-Carboniferous boundary in the Armorican Massif (France). Am Mineral 101(11):2430–2442

Qiu KF, Deng J (2017) Petrogenesis of granitoids in the *Dewulu skarn* copper deposit: implications for the evolution of the Paleotethys ocean and mineralization in Western Qinling, China. Ore Geol Rev 90:1078–1098

Qiu KF, Yu HC, Wu MQ, Geng JZ, Ge XK, Gou ZY, Taylor RD (2019) Discrete Zr and REE mineralization of the Baerzhe rare-metal deposit, China. Am Mineral 104(10):1487–1502

Qiu KF, Yu HC, Deng J, McIntire D, Gou ZY, Geng JZ, Chang ZS, Zhu R, Li KN, Goldfarb R (2020) The giant Zaozigou Au-Sb deposit in West Qinling, China: magmatic- or metamorphic-hydrothermal origin? Miner Depos 55(2):345–362

Qiu KF, Yu HC, Hetherington C, Huang YQ, Yang T, Deng J (2021a) Tourmaline composition and boron isotope signature as a tracer of magmatic-hydrothermal processes. Am Mineral 106(7):1033–1044

Qiu KF, Deng J, Yu HC, Wu MQ, Wang Y, Zhang L, Goldfarb R (2021b) Identifying hydrothermal quartz vein generations in the Taiyangshan porphyry Cu-Mo deposit (West Qinling, China) using cathodoluminescence, trace element geochemistry, and fluid inclusions. Ore Geol Rev 128:103882

Richards JP (2011) High Sr/Y arc magmas and porphyry Cu±Mo±Au deposits: just add water. Econ Geol 106(7):1075–1081

Richards JP, Şengör AC (2017) Did Paleo-Tethyan anoxia kill arc magma fertility for porphyry copper formation? Geology 45(7):591–594

Rubatto D (2017) Zircon: the metamorphic mineral. Rev Mineral Geochem 83(1):261–295

Scaillet B, Holtz F, Pichavant M (2016) Experimental constraints on the formation of Silicic Magmas. Elements 12(2):109–114

Sillitoe RH (2005) Supergene oxidized and enriched porphyry copper and related deposits. Econ Geol 100:723–768

Sisson T, Grove T (1993) Experimental investigations of the role of H_2O in calc-alkaline differentiation and subduction zone magmatism. Contrib Mineral Petrol 113(2):143–166

Sláma J, Košler J, Condon DJ, Crowley JL, Gerdes A, Hanchar JM, Horstwood MS, Morris GA, Nasdala L, Norberg N (2008) Plešovice zircon—a new natural reference material for U-Pb and Hf isotopic microanalysis. Chem Geol 249(1–2):1–35

Spencer CJ, Kirkland CL, Taylor RJM (2016) Strategies towards statistically robust interpretations of in situ U-Pb zircon geochronology. Geosci Front 7(4):581–589

Stacey JS, Kramers JD (1975) Approximation of terrestrial lead isotope evolution by a two-stage model. Earth Planet Sci Lett 26:207–221

Sui JX, Li JW, Wen G, Jin XY (2017) The Dewulu reduced Au-Cu skarn deposit in the Xiahe-Hezuo district, West Qinling orogen, China: Implications for an intrusion-related gold system. Ore Geol Rev 80:1230–1244

Szopa K, Sałacińska A, Gumsley AP, Chew D, Petrov P, Gawęda A, Zagórska A, Deput E, Gospodinov N, Banasik K (2020) Two-stage late Jurassic to early cretaceous hydrothermal activity in the Sakar unit of Southeastern Bulgaria. Minerals 10(3):266

Tollan P, Hermann J (2019) Arc magmas oxidised by water dissociation and hydrogen incorporation in orthopyroxene. Nat Geosci 12(8):667–671

Uchida E, Endo S, Makino M (2007) Relationship between solidification depth of granitic rocks and formation of hydrothermal ore deposits. Resour Geol 57(1):47–56

Utsunomiya S, Palenik CS, Valley JW, Cavosie AJ, Wilde SA, Ewing RC (2004) Nanoscale occurrence of Pb in an Archean zircon. Geochim Cosmochim Acta 68(22):4679–4686

Valley JW, Reinhard DA, Cavosie AJ, Ushikubo T, Lawrence DF, Larson DJ, Kelly TF, Snoeyenbos DR, Strickland A (2015) Nano- and micro-geochronology in Hadean and Archean zircons by atom-probe tomography and SIMS: new tools for old minerals. Am Mineral 100(7):1355–1377

White LT, Ireland TR (2012) High-uranium matrix effect in zircon and its implications for SHRIMP U-Pb age determinations. Chem Geol 306–307:78–91

Whitehouse MJ, Kamber BS (2002) On the overabundance of light rare earth elements in terrestrial zircons and its implication for Earth's earliest magmatic differentiation. Earth Planet Sci Lett 204(3–4):333–346

Whitehouse MJ, Kusiak M, Wirth R, Kumar GR (2017) Metallic Pb nanospheres in ultra-high temperature metamorphosed zircon from southern India. Mineral Petrol 111(4):467–474

Widmann P, Davies J, Schaltegger U (2019) Calibrating chemical abrasion: its effects on zircon crystal structure, chemical composition and UPb age. Chem Geol 511:1–10

Wiedenbeck M, Alle P, Corfu F, Griffin W, Meier M, Fv O, Av Q, Roddick J, Spiegel W (1995) Three natural zircon standards for U-Th-Pb, Lu-Hf, trace element and REE analyses. Geostand Newsl 19(1):1–23

Xian H, Zhu J, Tan W, Tang H, Liu P, Zhu R, Liang X, Wei J, He H, Teng HH (2019) The mechanism of defect induced hydroxylation on pyrite surfaces and implications for hydroxyl radical generation in prebiotic chemistry. Geochim Cosmochim Acta 244:163–172

Xu Y, Gu L, Li Y, Mo B, Lin Y (2018) Combination of focused ion beam (FIB) and microtome by ultrathin slice preparation for transmission electron microscopy (TEM) observation. Earth Planets Space 70(1):1–6

Yang LQ, Deng J, Dilek Y, Qiu KF, Ji XZ, Li N, Taylor RD, Yu JY (2015a) Structure, geochronology, and petrogenesis of the Late Triassic *Puziba granitoid* dikes in the Mianlue suture zone, Qinling Orogen, China. Geol Soc Am Bull 11(12):1831–1854

Yang LQ, Deng J, Qiu KF, Ji XZ, Santosh M, Song KR, Song YH, Geng JZ, Zhang C, Hua B (2015b) Magma mixing and crust–mantle interaction in the Triassic monzogranites of Bikou Terrane, central China: Constraints from petrology, geochemistry, and zircon U–Pb–Hf isotopic systematic. J Asian Earth Sci 98:320–341

Yu HC, Guo CA, Qiu KF, McIntire D, Jiang GP, Gou ZY, Geng JZ, Pang Y, Zhu R, Li NB (2019) Geochronological and geochemical constraints on the formation of the Giant Zaozigou Au-Sb deposit, West Qinling, China. Minerals 9(1):37

Yu HC, Qiu KF, Nassif MT, Geng JZ, Sai SX, Duo DW, Huang YQ, Wang J (2020a) Early orogenic gold mineralization event in the West Qinling related to closure of the Paleo-Tethys Ocean-Constraints from the *Ludousou gold* deposit, central China. Ore Geol Rev 117:103217

Yu HC, Qiu KF, Sai SX, McIntire DC, Pirajno F, Duo DW, Miggins DP, Wang J, Jia RY, Wu MQ (2020b) Paleo-tethys late triassic orogenic gold mineralization recorded by the Yidi'nan gold deposit, West Qinling, China. Ore Geol Rev 116:103211

Zhang BT, Wu JQ, Ling HF, Chen PR (2010) Magma-dynamic evidence for indosinian cycle emplacement of the qitianling granite batholith in Nanling range, Sourth China: reply and discussion to comments by Prof. Zhu Jinchu et al. Geol J China Univ 16(3):397

Zimmer MM, Plank T, Hauri EH, Yogodzinski GM, Stelling P, Larsen J, Singer B, Jicha B, Mandeville C, Nye CJ (2010) The role of water in generating the Calc-alkaline trend: new volatile data for aleutian magmas and a new Tholeiitic Index. J Petrol 51(12):2411–2444

Zou X, Qin K, Han X, Li G, Evans NJ, Li Z, Yang W (2019) Insight into zircon REE oxy-barometers: a lattice strain model perspective. Earth Planet Sci Lett 506:87–96